Quantification of the human–structure interaction effect through full-scale dynamic testing: The Folke Bernadotte Bridge

Structures 55 (2023) 2249–2265

Contents lists available at ScienceDirect

Structures

journal homepage: www.elsevier.com/locate/structures

Quantification of the human–structure interaction effect through full-scale dynamic testing: The Folke Bernadotte Bridge

D. Colmenares [a,*], G. Costa [b,c], M. Civera [d], C. Surace [d], R. Karoumi [a]

[a] Division of Structural Engineering and Bridges, KTH Royal Institute of Technology, 10044, , Stockholm, Sweden
[b] Department of Architecture, Built Environment and Construction Engineering, Politecnico Di Milano, Piazza Leonardo da Vinci, 32, 20133 Milan, Italy
[c] Department 7: Safety of Structures, BAM Federal Institute for Materials Research and Testing, Unter den Eichen 87, Steglitz, 12205 Berlin, Germany
[d] Department of Structural, Geotechnical and Building Engineering, Di Torino, C. Duca Degli Abruzzi, 24, 10129 Turin, Italy

ARTICLE INFO

Keywords:
Human–structure interaction
Footbridges
Human model

ABSTRACT

An analytical expression for the frequency response function of a coupled pedestrian-bridge system is presented and evaluated using an experimental measurement campaign performed on the Folke Bernadotte Bridge in Stockholm, Sweden. A finite element model and the modal models that consider the human–structure interaction effect are calibrated with respect to the measurements. The properties of the spring–mass–damper model representing the pedestrians were identified, considering the different structural modes of the system. Good agreement was obtained between the experimental and theoretical frequency response functions. A sensitivity analysis of the obtained solution was performed, validating the determined analytical expression for the frequency response function of the coupled pedestrian-bridge system that takes into account the human–structure interaction effect.

1. Introduction

Footbridges are being designed with more innovative and cutting-edge features and with shapes that make them more slender and lighter [1]. Hence, dynamic effects are becoming more important in such systems [2]. For example, wind loads that can introduce vortex-induced vibrations, wind flutter and crowd loading scenarios may lead to undesirable vibrations and potentially produce resonance conditions that may compromise the serviceability limit state of the system [3]. As shown in [4,5], the human–structure interaction (HSI) effect can strongly affect the dynamic performance of the system due to the added damping and the frequency shift effect. This is particularly important considering that the current design guidelines and recommendations that address the dynamic performance of footbridges [3,6–14] do not provide any information regarding added damping or the frequency shift phenomena due to the HSI effect.

Moreover, despite the many different HSI formulations [15–27], specialised software would be required to implement the state-of-the-art formulations. Furthermore, it is important to consider the uncertainty of such systems in the design phase. Van Nimmen et al. [28] show that uncertainty in the dynamic properties of a footbridge is unavoidable and that even with a detailed finite element model (FEM), deviations can be expected. This highlights the need for a design methodology that is less sensitive to small variations in the inherent dynamic properties of the system. Additionally, the guidelines address the subjective character of the serviceability limit state of the comfort criteria by (i) establishing ranges of critical frequencies and vibration responses rather than absolute limits and (ii) classifying the system according to the desired comfort limit and expected traffic conditions. In addition, different models for studying the walking load action were presented in [29], suggesting that the design procedure can be validated through tests of the system in order to fully validate the design. Additionally, the serviceability criteria related to the vibration level of footbridges is an ongoing research subject [30,31], adding complexity to the design process. A study of the pedestrian loading for restricted traffic conditions using spectral load models and current design guidelines is presented in [32], and a benchmark dataset that can be used to test and validate crowd load models is presented in [33].

A simplified method that can be used to consider the HSI effect can be found in [34]; it may lead to a good conservative estimate of the structural acceleration response. An equivalent force model can be found in [35]; it is limited to bridges with simple supported mode shapes. It is clear that there is a need for a simplified approach that can take into account the HSI effect. A review of human-induced vibrations can be found in [36]; it is focused on the different time-domain load models.

* Corresponding author.
E-mail address: dancol@kth.se (D. Colmenares).

https://doi.org/10.1016/j.istruc.2023.06.133
Received 3 April 2023; Received in revised form 20 June 2023; Accepted 27 June 2023
Available online 11 July 2023

The main contribution of this work is to provide a closed-form expression for the frequency response functions (FRFs) of a coupled pedestrian-bridge system, along with the corresponding experimental verification, taking into account the HSI effect. The proposed formulation requires less computation time, and it is tested and compared with an FEM and Caprani's formulation [17]. This work presents the experimental campaign carried out on the Folke Bernadotte Bridge to characterise the dynamic properties of the system with and without pedestrians. The FEM of the bridge is developed and calibrated such that the difference between the theoretical and experimental FRFs is minimised when no pedestrians are on the bridge. This is done by adjusting the assumed elastic boundary conditions and material properties while fixing the identified modal damping ratios. Furthermore, a test with uniformly distributed pedestrians on the bridge is presented, and the calibration procedure is repeated to adjust the assumed Single Degree of Freedom (SDOF) human model in the FEM by using the proposed expression for the FRF and using Caprani's formulation [17], considering the experimentally identified mode shapes. There is agreement among the analytical solution, Caprani's formulation, the calibrated FEM and the experimental results.

2. Modelling framework for the HSI effect

To simulate human-induced vibrations in a coupled pedestrian-bridge system, different approaches can be found in the literature that are formulated in the modal domain or using FE-based methods. In this section, Venuti's formulation [18], Caprani's formulation and the analytical expression for the FRFs of a coupled pedestrian-bridge system are introduced. Furthermore, in this work, Caprani's formulation [17], the closed-form solution and the FEM in which pedestrians have been modelled are compared to the measurement results.

2.1. Venuti's formulation

In Venuti's formulation [18], the supporting structure is modelled as an SDOF system and has the dynamic properties, i.e. mass, damping and stiffness, of the unoccupied structure; each pedestrian in the crowd is modelled as an SDOF system with its own dynamic properties, i.e. mass, damping and stiffness. The HSI effect is quantified by evaluating the effect of the N_p pedestrians on the dynamic properties and the changes in the FRFs of the coupled system. In this way, the dynamic system is established as follows:

$$\mathbf{M}\ddot{\mathbf{X}} + \mathbf{C}\dot{\mathbf{X}} + \mathbf{K}\mathbf{X} = \mathbf{F}, \tag{1}$$

where the mass, damping and stiffness matrices are defined as

$$\mathbf{M} = \begin{bmatrix} m_{b,n} & 0 & \cdots & 0 \\ 0 & m_{p,1} & & 0 \\ \vdots & & \ddots & \vdots \\ 0 & 0 & \cdots & m_{p,N_b} \end{bmatrix},$$

$$\mathbf{C} = \begin{bmatrix} c_{b,n} + \sum_{r=1}^{N_p} c_{p,r}\phi_n^2(x_{p,r}) & -c_{p,1}\phi_n(x_{p,1}) & \cdots & -c_{p,N_p}\phi_n(x_{p,N_p}) \\ -c_{p,1}\phi_n(x_{p,1}) & c_{p,1} & & 0 \\ \vdots & & \ddots & \vdots \\ -c_{p,N_p}\phi_n(x_{p,N_p}) & 0 & \cdots & c_{p,N_p} \end{bmatrix},$$

$$\mathbf{K} = \begin{bmatrix} k_{b,n} + \sum_{r=1}^{N_p} k_{p,r}\phi_n^2(x_{p,r}) & -k_{p,1}\phi_n(x_{p,1}) & \cdots & -k_{p,N_p}\phi_n(x_{p,N_p}) \\ -k_{p,1}\phi_n(x_{p,1}) & k_{p,1} & & 0 \\ \vdots & & \ddots & \vdots \\ -k_{p,N_p}\phi_n(x_{p,N_p}) & 0 & \cdots & k_{p,N_p} \end{bmatrix} \tag{2}$$

and the displacement and force vectors are defined as

$$\mathbf{X} = \begin{bmatrix} X_{b,n} \\ X_{p,1} \\ \vdots \\ X_{p,N_p} \end{bmatrix}, \quad \mathbf{F} = \begin{bmatrix} P_n(t) \\ 0 \\ \vdots \\ 0 \end{bmatrix}, \tag{3}$$

where $m_{b,n}$, $c_{b,n}$ and $k_{b,n}$ represent the modal mass ($m_{b,n} = \int_0^L \gamma(x)\phi_n^2(x)\,dx$, $\gamma(x)$ indicates the linear density), damping and stiffness of the supporting structure for the given mode n, respectively. The parameter $x_{p,r}$ represents the coordinate of the location of the considered pedestrian r. The parameters $m_{p,r}$, $c_{p,r}$ and $k_{p,r}$ represent the mass, damping and stiffness of the general considered pedestrian r. Finally, ϕ_n and $P_n(t) = \sum_{r=1}^{N_p} F_{p,r}(t)\phi_n(x_{p,r})$ are defined as the unit-normalised (mode n) mode shape of the structure and the modal load, respectively. The term $F_{p,r}(t)$ indicates the ground reaction forces. Both the mode shape and the modal load can be analytically obtained by using the closed-form frameworks outlined in [37,38] for continuous beam systems over elastic supports. In this formulation, the system's matrices are symmetric and one single structural mode n is considered.

2.2. Caprani's formulation

Caprani and Ahmadi [17] investigated the crowd–structure interaction and the pedestrian action considering the moving force (MF), the moving mass (MM) and the spring–mass–damper (SMD) model. The main difference between the approaches presented in [17,18] is that Venuti et al. [18] express the interaction forces as the sum of the elastic and damping forces of the pedestrian system instead of considering the inertial forces used in [17]. The mass, damping and stiffness matrices of Caprani's formulation are defined as follows:

$$\mathbf{M} = \begin{bmatrix} \mathbf{I}_{NxN} & \mathbf{M}_{12} \\ \mathbf{0}_{1xN} & \mathbf{m}_p \end{bmatrix}, \quad \mathbf{C} = \begin{bmatrix} \mathbf{C}_{11} & \mathbf{0}_{1xN} \\ \mathbf{C}_{21} & \mathbf{c}_p \end{bmatrix},$$
$$\mathbf{K} = \begin{bmatrix} \mathbf{K}_{11} & \mathbf{0}_{1xN} \\ \mathbf{K}_{21} & \mathbf{k}_p \end{bmatrix}, \quad \mathbf{F} = \begin{bmatrix} \mathbf{P}_{Nx1} \\ \mathbf{0}_{N_p x1} \end{bmatrix}, \tag{4}$$

where N is the number of the bridge modes considered in the analysis, N_p is the number of pedestrians, the terms $\mathbf{M}_{12}$, $\mathbf{C}_{21}$ and $\mathbf{K}_{21}$ represent the pedestrian-bridge coupling terms, $\mathbf{m}_p$, $\mathbf{c}_p$ and $\mathbf{k}_p$ represent the pedestrian dynamic properties and $\mathbf{P}$ represents the applied modal load on the bridge. The aforementioned parameters are defined as follows:

$$\begin{aligned} \mathbf{M}_{12}[1,\ldots,N;i] &= m_{p,i}\phi(v_i t), & \mathbf{C}_{11} &= diag[2\zeta_j\omega_j], \\ \mathbf{C}_{21} &= -c_{p,i}\phi^T(v_i t), & \mathbf{K}_{11} &= diag[\omega_j], \\ \mathbf{K}_{21}[1,\ldots,N;i] &= -k_{p,i}\phi^T(v_i t), & P_j &= G(t)\phi_j(vt), \\ \mathbf{m}_p = diag[m_{p,i}], & & \mathbf{c}_p = diag[c_{p,i}], & \quad \mathbf{k}_p = diag[k_{p,i}], \end{aligned} \tag{5}$$

where $m_{p,i}$, $c_{p,i}$ and $k_{p,i}$ represent the mass, damping and stiffness of the ith pedestrian, respectively. The term v_i is the velocity of the corresponding pedestrian i, and ϕ represents the mode shape vector. The terms ζ_j and ω_j indicate the damping and the circular natural frequency of the bridge associated with mode j. Finally, $G(t)$ is the generalised force function, i.e. the vertical force generated by the walking pedestrians. In this way, Caprani's formulation makes it possible to consider multiple modes of the supporting structure, taking into account the coupling terms between different structural modes due to the presence of the pedestrians' SMD models.

2.3. Closed-form solution of the HSI effect

An analytical framework that can be used to quantify the HSI effect based on Venuti's formulation [18] can be developed. Following Venuti's formulation [18], in which a single mode of vibration n of the coupled system is considered, with N_p SDOFs that represent the pedestrians arbitrarily distributed over a general continuous beam [37–40], the FRF H_{HSI} of the coupled pedestrian-bridge system can be obtained through the matrix condensation of the original system in the frequency domain:

$$Z_{HSI} = \mathbf{Z}_{(1,1)} - \mathbf{Z}_{(1,2)}\mathbf{Z}_{(2,2)}^{-1}\mathbf{Z}_{(2,1)}, \tag{6}$$

where

$$\mathbf{Z}_{(1,1)} = \left[-\omega^2 m_{\mathrm{b},n} + \mathrm{i}\omega\left(c_{\mathrm{b},n} + \sum_{r=1}^{N_\mathrm{p}} c_{\mathrm{p},r}\phi_n^2(x_{\mathrm{p},r})\right) + k_{\mathrm{b},n} + \sum_{r=1}^{N_\mathrm{p}} k_{\mathrm{p},r}\phi_n^2(x_{\mathrm{p},r})\right]_{1\times 1},$$
$$\mathbf{Z}_{(1,2)} = \left[-\phi_n(x_{\mathrm{p},r})(\mathrm{i}\omega c_{\mathrm{p},r} + k_{\mathrm{p},r})\right]_{1\times N_\mathrm{p}},$$
$$\mathbf{Z}_{(2,1)} = \mathbf{Z}_{(1,2)}^{\mathrm{T}},$$
$$\mathbf{Z}_{(2,2)} = \mathrm{diag}\left[-\omega^2 m_{\mathrm{p},r} + \mathrm{i}\omega c_{\mathrm{p},r} + k_{\mathrm{p},r}\right]_{N_\mathrm{p}\times N_\mathrm{p}}, \tag{7}$$

where Z_{HSI} is the impedance function of the coupled pedestrian-bridge system. Finally, the frequency response function of the coupled bridge system H_{HSI} is

$$\mathrm{H}_{\mathrm{HSI}} = 1/\left(-\omega^2 m_{\mathrm{b},n} + \mathrm{i}\omega\left(c_{\mathrm{b},n} + \sum_{r=1}^{N_\mathrm{p}} c_{\mathrm{p},r}\phi_n^2(x_{\mathrm{p},r})\right) + k_{\mathrm{b},n} + \sum_{r=1}^{N_\mathrm{p}} k_{\mathrm{p},r}\phi_n^2(x_{\mathrm{p},r}) + \sum_{r=1}^{N_\mathrm{p}} -\phi_n^2(x_{\mathrm{p},r})\frac{(\mathrm{i}\omega c_{\mathrm{p},r} + k_{\mathrm{p},r})^2}{-\omega^2 m_{\mathrm{p},r} + \mathrm{i}\omega c_{\mathrm{p},r} + k_{\mathrm{p},r}}\right). \tag{8}$$

Taking as a common factor the modal stiffness of the bridge $k_{\mathrm{b},n}$ and considering the definitions

$$k_{\mathrm{b},n} = \omega_{\mathrm{b},n}^2 m_{\mathrm{b},n}, \qquad k_{\mathrm{p},r} = \omega_{\mathrm{p},r}^2 m_{\mathrm{p},r},$$
$$c_{\mathrm{b},n} = 2\zeta_{\mathrm{b},n}\omega_{\mathrm{b},n} m_{\mathrm{b},n}, \qquad c_{\mathrm{p},n} = 2\zeta_{\mathrm{p},n}\omega_{\mathrm{p},n} m_{\mathrm{p},n}, \tag{9}$$

where $\omega_{\mathrm{b},n}$, $\omega_{\mathrm{p},r}$, $\zeta_{\mathrm{b},n}$ and $\zeta_{\mathrm{p},n}$ refer to the (mode n) circular natural frequency of the supporting structure, the circular natural frequency of pedestrian r, the damping ratio of the considered mode n of the structure and the damping ratio of the pedestrian r, respectively, H_{HSI} can be written as

$$\mathrm{H}_{\mathrm{HSI}} = \frac{1}{k_{\mathrm{b},n}} 1/\left(-\frac{\omega^2}{\omega_{\mathrm{b},n}^2} + \mathrm{i}\frac{\omega}{\omega_{\mathrm{b},n}}\left(2\zeta_{\mathrm{b},n} + \sum_{r=1}^{N_\mathrm{p}} 2\zeta_{\mathrm{p},r}\frac{m_{\mathrm{p},r}}{m_{\mathrm{b},n}}\frac{\omega_{\mathrm{p},r}}{\omega_{\mathrm{b},n}}\phi_n^2(x_{\mathrm{p},r})\right) + 1 + \sum_{r=1}^{N_\mathrm{p}} \frac{m_{\mathrm{p},r}}{m_{\mathrm{b},n}}\frac{\omega_{\mathrm{p},r}^2}{\omega_{\mathrm{b},n}^2}\phi_n^2(x_{\mathrm{p},r}) - \sum_{r=1}^{N_\mathrm{p}} \frac{m_{\mathrm{p},r}}{m_{\mathrm{b},n}}\frac{\omega_{\mathrm{p},r}^2}{\omega_{\mathrm{b},n}^2}\beta_{\mathrm{p},r}\phi_n^2(x_{\mathrm{p},r})\right), \tag{10}$$

where $\beta_{\mathrm{p},r}$ is defined as

$$\beta_{\mathrm{p},r} = \frac{(\mathrm{i}\frac{\omega}{\omega_{\mathrm{p},r}}2\zeta_{\mathrm{p},r} + 1)^2}{(-\frac{\omega^2}{\omega_{\mathrm{p},r}^2} + \mathrm{i}\frac{\omega}{\omega_{\mathrm{p},r}}2\zeta_{\mathrm{p},r} + 1)}. \tag{11}$$

The determined analytical expression will be used in this work to quantify the HSI effect.

3. Experimental testing

3.1. Introduction to the bridge

The Folke Bernadotte Bridge is an important walking and cycling bridge across the Djurgårdsbrunn Bay in Stockholm, Sweden. The pedestrian bridge was inaugurated on 19 September 2019, and it connects the southern and northern parts of the park of Djurgården. An image of the Folke Bernadotte Bridge is given in Fig. 1. The bridge is named after the nobleman, diplomat and negotiator Folke Bernadotte, who was appointed as the UN's first mediator following the Second World War. The construction of the bridge was initiated in June 2018. Its supports and abutments are made out of concrete, and they are hidden under the ground. The steel part of the bridge was produced in a factory and installed in 2019. The total span of 97 m is covered by a single-arch bridge made of stainless steel. The structural system was designed as a 3D frame. The structural system consists of three main continuous tubes, two at the deck surface of cross-section CHS355.6X12.5 and one on the lower level of cross-section CHS298.5X25, within CHS355.6X25. The three components are linked by inclined members within cross-section CHS193.7X5.6 that form the truss system. A series of longitudinal trapezoidal components and transverse rectangular elements support the wooden deck. The rectangular components are welded to the lateral pipes, while the longitudinal components are connected to the transversal components. Furthermore, additional diagonal pieces are positioned across the transversal span to offer major stiffness. Along with the maritime traffic requirements, the bridge provides a sail-free height of 3 m. Figs. 2 and 3 provide plan and elevation views of the bridge, respectively.

Fig. 1. The Folke Bernadotte Bridge in Djurgården, Stockholm, Sweden.

The foundations are here referred as support 1 (left hand side) and support 2 (right hand side). The support 1 consists of a trapezoidal shaped reinforced concrete block with a length of 15.82 m and a varying depth from 0.9 m to 0.8 m, following the shape of bridge. Support 1 is laying over the bedrock located at −1.2 m and a new gravel material layer having an elastic modulus of 50 MPa (having a friction angle of 45°). The support 2 consists of a trapezoidal reinforced concrete block with a length of 16.82 m and a varying depth from 1.552 m to 1.4 m over a layer of clay of 2.4 m of depth with a characteristic shear strength of 10 kPa, followed by a friction material of 1.0 m of depth with an elastic modulus of 30 MPa (having a friction angle of 38°) and finally the bedrock. The load transfer between the trapezoidal reinforced concrete block and the bedrock is made by 12 inclined end bearing steel piles (along and transversally with respect to the axis of the bridge) supported in the bedrock so that negligible settlements are expected. However, the Soil–Structure Interaction (SSI) effect is neglected in this study, and it is out of the scope of the work [41].

3.2. Hammer tests: instrumentation and loading

The Folke Bernadotte Bridge was subjected to two sets of experimental tests on 23 March 2021 (day one) and 11 May 2021 (day two). Day one was dedicated to capturing the vibrational behaviour of the (almost) unloaded structure. On day two, the dynamic response of the structure was evaluated both with and without a pedestrian load.

The ambient conditions were recorded on day one as sunny, with a temperature of 19 °C and a light wind from the west. The temperature and wind speed were not directly measured on day two but recordings from nearby weather stations suggest that the temperature was about 23 °C, with a light wind from the east. In both cases, no sudden intraday changes were detected.

The experimental datasets for the unloaded footbridge include hammer, running, walking and jumping tests. In general, for bridge system identification (SI), these are the dominant modes of the global structural behaviour [42,43]. Furthermore, these modes are also the closest to the frequencies of the human system and human walking and running paces; thus, for these modes, the structure is most prone to exhibiting high levels of vibrations and interactions, i.e. the HSI effect. For these reasons, the hammer test was selected for the input–output SI of the target structure. Hence, only this type of test will be described in detail for both the unloaded and loaded cases.

The datasets of interest consist of eight series of hammer hits, as described in Table 1. Series 1 to 4 were recorded on the first day of experiments (23 March, only the unloaded case), while series 5 to 8

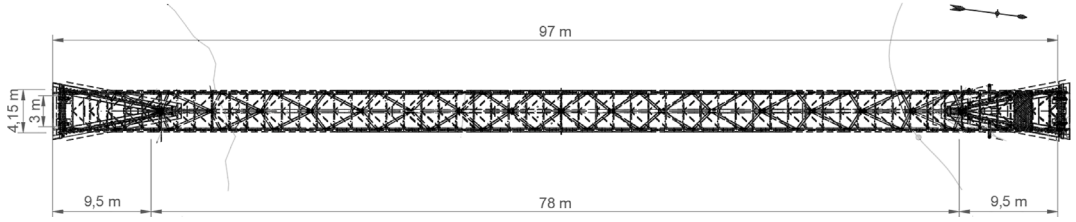

Fig. 2. Plan view of the Folke Bernadotte Bridge.

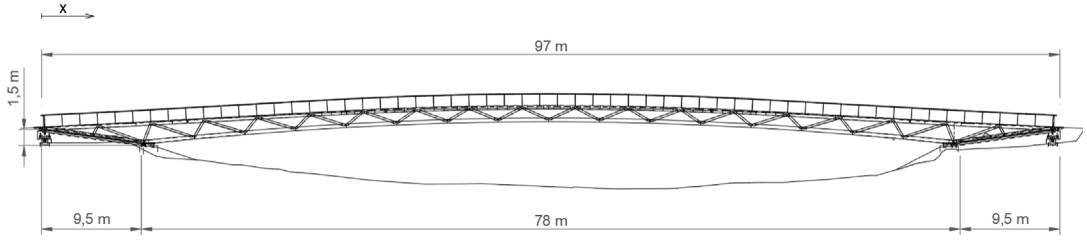

Fig. 3. Elevation view of the Folke Bernadotte Bridge.

Table 1
Details of the experimental campaign (hammer tests).

Series ID	Date	Carried human load (static)	Sensor layout	Excitation source location
1	23 March 2021	2 operators	layout A	E1
2	23 March 2021	2 operators	layout A	E2
3	23 March 2021	2 operators	layout B	E1
4	23 March 2021	2 operators	layout B	E2
5	11 May 2021	2 operators	layout C	E2
6	11 May 2021	2 operators	layout C	E2
7	11 May 2021	2 operators + 33 pedestrians	layout C	E2
8	11 May 2021	2 operators + 33 pedestrians	layout C	E2

were acquired during the second day (11 May, loaded and unloaded cases).

For series 1 to 6, only two operators, who were needed to perform the hammer hits at two distinct locations, were allowed on the bridge deck at the two points E1 and E2. In this case, the bridge can be approximated as unloaded.

For series 7 and 8, the bridge was loaded with 35 bystanders, with all of them standing still and equally spaced (1.5 m) along the bridge line, as shown in Fig. 4(a). The total additional mass was 2794.7 kg, with an average pedestrian weight equal to 79.85 ± 14.90 kg ($\mu \pm \sigma$); the weights of the pedestrians ranged from a minimum of 56.3 kg to a maximum of 110.0 kg. These pedestrians were intended to act as both localised additional masses and additional dampeners (dynamic vibration absorbers). As the Folke Bernadotte Bridge is particularly lightweight even by the standards of pedestrian bridges (with a density of about 1000 kg per linear metre), the designed experiment was expected to noticeably affect its modal properties.

Series 1 and 2 used the sensor layout A, while series 3 and 4 used the alternative layout B. Both layouts (portrayed in Figs. 5(a) and 5(b), respectively) included 14 vertical output channels, denoted by a1 to a14, plus three horizontal output channels (a15 to a17); the results from the horizontal output channels are not reported here, as this study focus solely on the vertical dynamics of the slender footbridge. Series 5 to 8 used the sensor layout C, with a reduced number of vertical acquisition channels (a1 to a6) and no horizontal recordings. This third layout consisted of six sensors placed in the same locations as a2, a3, a4, a11, a12 and a13 in layout B (see Fig. 5(c)). This choice was made due to the necessity of moving the external modules of the acquisition setup, which were initially placed on the bridge at its midpoint, away from this location to accommodate the standing pedestrians. This specific choice introduced some slight limitations in the identification of the mode shapes, which will be discussed in more detail in the next subsection.

In all layouts (A, B and C), each channel corresponded to a PCB 393A03 uniaxial accelerometer (Fig. 4(b)). These accelerometers have a sensitivity of 1 V/g and a frequency range from 0.5 Hz to 2 kHz, and they can record a maximum acceleration of 5 g. A very high sampling frequency (f_s = 1200 Hz) was set for the recordings; the signals were then subsampled to f_s^* = 200 Hz in post-processing.

The input signals were acquired as force recordings using one Dytran 5803A instrumented sledgehammer (Fig. 4(c)). Two distinct locations were used for the excitation source: the aforementioned E1 (series 1 and 3) and E2 (series 2, 4 and 5 to 8) points, as indicated in Fig. 5. Thus, the first four signals contain all the possible permutations of the placements of two input sensors and two output sensors. The input and output signals were all synchronised thanks to three external modules.

For each series, all the hammer hits were performed consecutively in one recording and without interruption. However, some hammer hits generated corrupted data at one or more output channels. This handful of signals of hammer hits (two out of twelve in Series 1, two out of eleven in Series 2, one out of nine in Series 3, and two out of eleven in Series 4) were thus discarded according to engineering judgement. In terms of cumulative coherence, the FRFs of these signals proved to be much less reliable than the other signals, which all scored more than 98%.

3.3. Hammer tests: post-processing of the experimental results

The experimental data have been investigated in terms of the absolute value and phase angle of accelerance FRFs. The output channels directly recorded the bridge vibrations in units of m/s^2, while the data from the instrumented hammer were originally in units of kN and were then multiplied by 10^3 in post-processing. Both the output and input signals have been filtered (Butterworth filter of order 3), bandpassing between 0.5 and 12 Hz. The lower cut-off frequency $f_{c,1}$ was needed to remove the very-low-frequency deviations. $f_{c,1}$ is well below the first mode. The upper cut-off frequency $f_{c,2}$ was set according to the modes of interest. Each hammer hit was isolated from the rest of the signal and investigated on its own. According to the suggestions of [44] (Chapter 13.8), the offset of each input and output signal was corrected by

(a) (b) (c)

Fig. 4. Photographs from the in situ survey on day two: (a) Pedestrians in position for the loaded case. (b) One of the accelerometers.

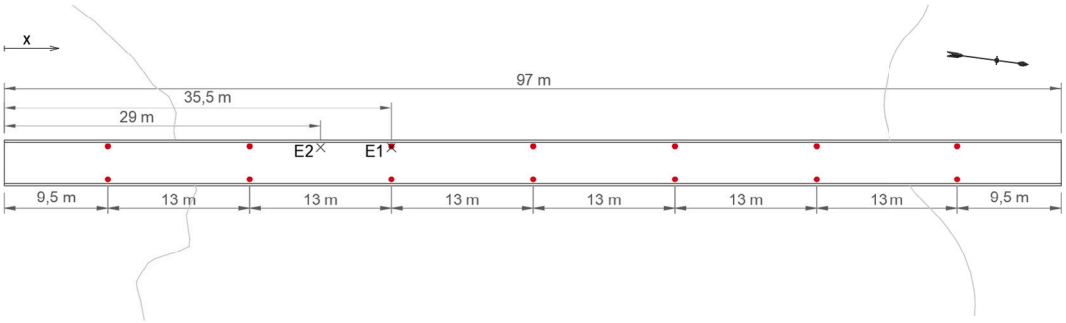

(a)

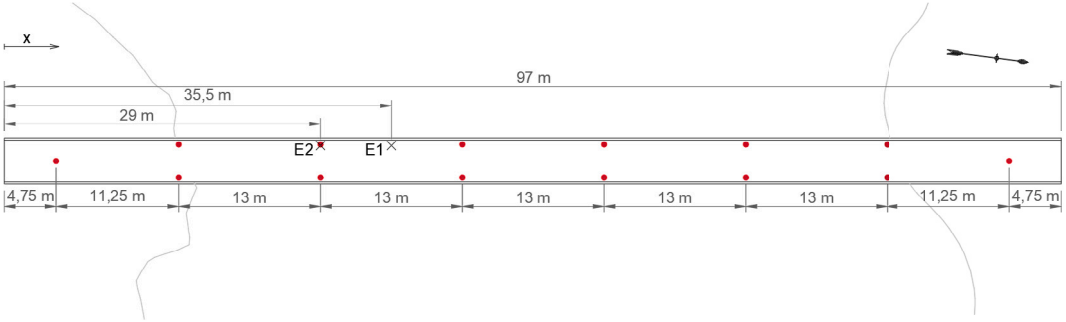

(b)

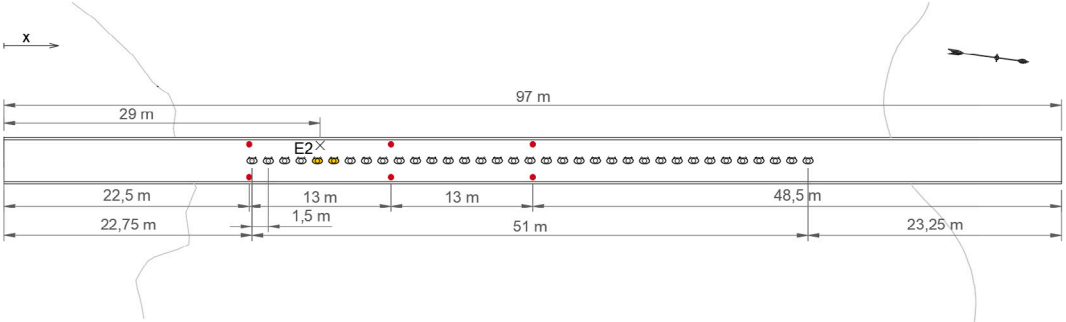

(c)

Fig. 5. Sensor layouts (a) A, (b) B and (c) C; the sensors are indicated by the red circles. For A and B, only the vertical output channels (a1 to a14) are shown. The black X's (E1 at 35.5 m from the south edge and E2 at 29 m) in (a) and (b) indicate the excitation sources, i.e. the locations where the hammer hits were applied. The locations of the 35 standing pedestrians are indicated in (c), with the two operators highlighted. Units of [m] are used. (For interpretation of the references to colour in this figure legend, the reader is referred to the web version of this article.)

subtracting the mean of each signal and performing detrending where and if needed. The noise floor of the signals was removed using an exponential window (Fig. 6(b)), which was applied for each hammer hit at all output channels and to the input as well (to avoid distortions in the damping estimates). The force signals were windowed with a Gaussian time window as well to remove the after-impact measurement

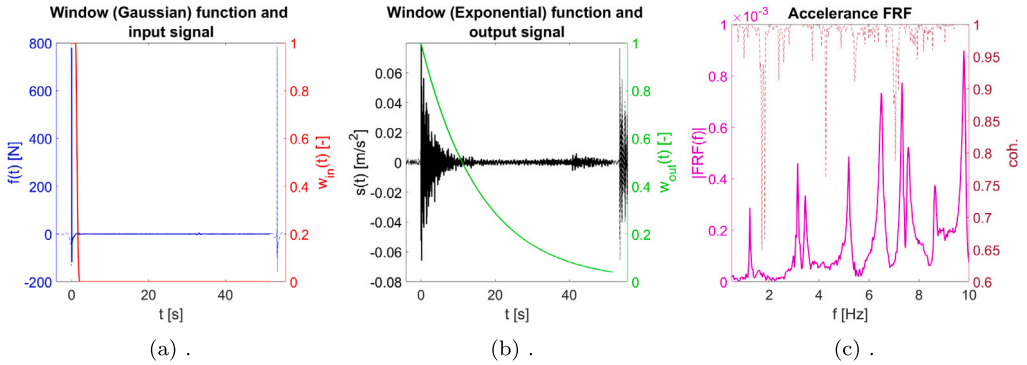

Fig. 6. Examples of (a) input ($f(t)$ [N]) and (b) output ($s(t)$ [m/s^2]) signals with their corresponding windowing functions, plus (c) the resulting FRF. The dashed lines in (a) at the beginning and end of the signal indicate the previous and following hammer hits from the same recording.

Table 2
Identified natural frequencies (in Hz) and damping ratios (in %).

Mode	Series 1	Series 2	Series 3	Series 4	Series 5	Series 6	Series 7	Series 8
f_1	1.57	1.57	1.53	1.53	1.69	1.67	1.46	1.46
ζ_1	1.75	1.63	1.91	2.12	1.52	1.48	2.61	2.65
f_2	3.00	2.99	3.00	3.00	3.02	3.03	2.92	2.92
ζ_2	0.79	0.85	0.56	0.73	0.80	0.76	1.77	1.74
f_3	5.24	5.23	5.23	5.24	5.30	5.31	5.12	5.15
ζ_3	0.91	0.86	0.91	1.06	0.77	0.81	2.37	2.31

noise, as shown in Fig. 6(a). Fig. 6(c) shows an example of the resulting accelerance FRFs.

The estimated natural frequencies for the first three modes of the unloaded and loaded bridge are reported in Table 2. The damping ratios were compensated to account for the influence of the exponential window, which was intentionally applied to both the input and output channels following [44]. The differences in terms of damping ratio quantitatively reported in Table 2 can be also seen in Fig. 7. This shows a continuous wavelet transform (CWT) analysis (with a Morlet wavelet) performed on some examples of hammer hits taken from Series 5 (Fig. 7(a) - no pedestrians) and 7 (Fig. 7(b) - with pedestrians), respectively. These highlight that the response signals are consistent for hammer hits belonging to the same series. They also help in visualising what is reported in Table 2, that is to say, how the footbridge becomes much more damped due to the pedestrians. In fact, as the damping increases (due to the standing pedestrians acting as added dampers), the frequency content, especially at the higher frequencies, fades out much earlier.

Fig. 8 portrays the mode shapes of the same modes for the unloaded bridge and sensor layout A. The fitted functions for the experimental modes are given in Eq. (A.1). The fitting of the mode shapes was done using the nonlinear least squares method implemented in MATLAB, with acceptable values of the coefficient of determination (R^2). The eigensystem realisation analysis (ERA) algorithm [45] was used for the estimation of all these modal parameters.

In terms of mode shapes, the results were in agreement within the three different layouts. The modal assurance criterion (MAC) matrix between the first and second series of hammer hits (not reported here for brevity) showed a value always larger than 0.990 for all terms on the main diagonal and always lower than $1.8 \cdot 10^{-4}$ for all the remaining terms outside of it. That proves how the mode shapes captured with layout A are consistent among themselves. Similarly, for layout B, the MAC matrix between series 3 and 4 showed values always larger than 0.995 on the main diagonal and always lower than $2.1 \cdot 10^{-4}$ for the off-diagonal terms. On the other hand, Fig. 9 portrays the MAC matrices between the identified modes of interest extracted from the day two recordings. These correspond to the modes of vibration of the unloaded (Series 5 and 6) and loaded (Series 7 and 8) cases, taken for the same sensor arrangement (layout C). The eigenshapes of series 5 and 6 are so similar that their cross-MAC values are comparable to their respective auto-MAC values. The same can be said for the modes identified in series 7 and 8. On the other hand, the cross-MAC values between the unloaded (Series 5 and 6) and loaded (Series 7 and 8) cases show some minimal yet visible variations induced by human loading. In all cases, the relatively high values of the off-diagonal terms between the second mode and the other modes are due to the specific sensor layout, which is limited to one half of the bridge length. For this reason, the results from layout A were used to report the unloaded mode shapes (as depicted in Fig. 8).

4. Model calibration

4.1. Full-bridge FE model

A FEM of the Folke Bernadotte Bridge was created in Abaqus (copyright 2002–2020 Dassault Systémes Simulia Corp). For the sake of simplicity, the bridge was modelled in four portions and then assembled. Tie constraints were used in the model to account for full interaction, i.e. axial, shear and bending forces were transferred. The numerous bridge components were modelled as cubic Euler–Bernoulli B33 beam elements and accounted for the design dimensions and materials. The wooden deck and the railings were considered by adjusting the density of the steel members from 7850 kg/m^3 to 8800 kg/m^3. However, given the uncertainties of the looser timber pieces forming the supporting deck, the density parameter is further adjusted in the modal updating process in order to minimise the differences between the theoretical and experimental FRFs. The FEM of the Folke Bernadotte Bridge is depicted in Fig. 10.

The boundary conditions (BCs) at the six supports were investigated considering three different configurations. In the first configuration, as shown in Fig. 11a, the right lower support allows longitudinal displacements. In the second configuration, as shown in Fig. 11b, the right lower support does not allow longitudinal displacements. In the third configuration, as shown in Fig. 12, the longitudinal displacement of the boundary condition is considered using a linear spring with a stiffness k_1. Finally, the third configuration in which an elastic boundary condition is considered is used for update the model.

Pedestrians were modelled by assuming that an SDOF SMD system was linked to the two main tube beams of the bridge system. Consequently, two vertical parallel springs with half of the corresponding pedestrian stiffness and two vertical parallel dampers with half of the pedestrian damping are used. A schematic of the modelling approach is shown in Fig. 13a. For the Abaqus FEM, the proposed modelling approach is shown in Fig. 13b.

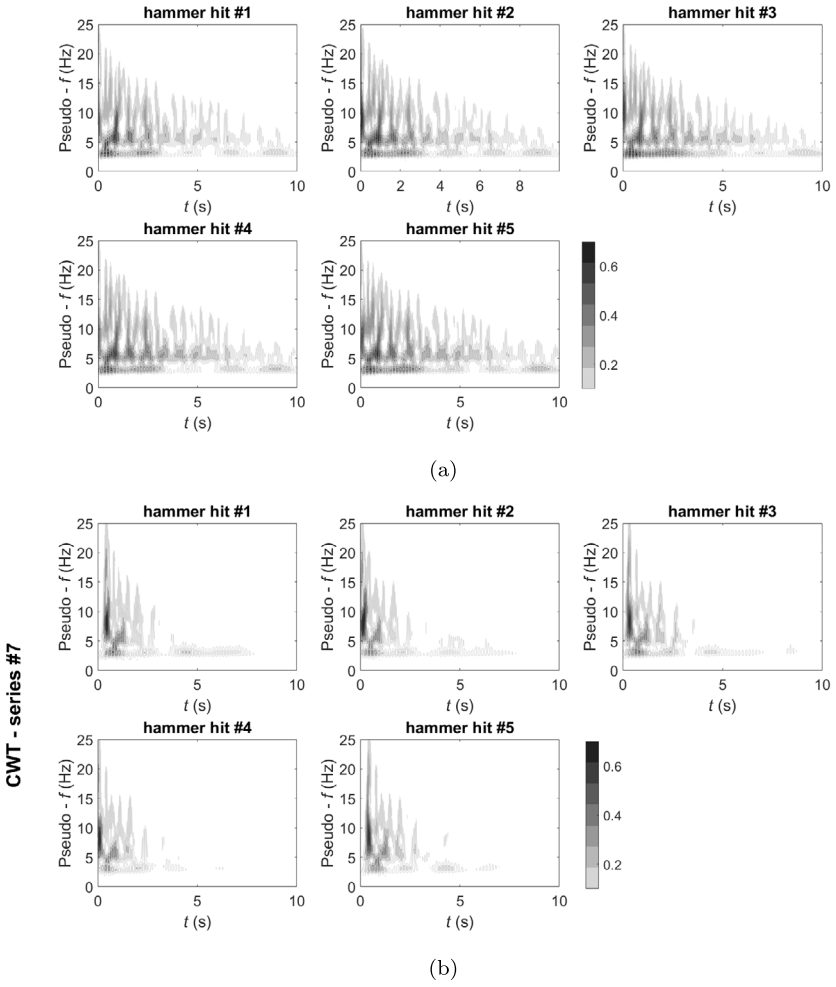

Fig. 7. CWT analysis for the hammer hits of (a) series 5 (no pedestrians) and (b) series 7 (with pedestrians).

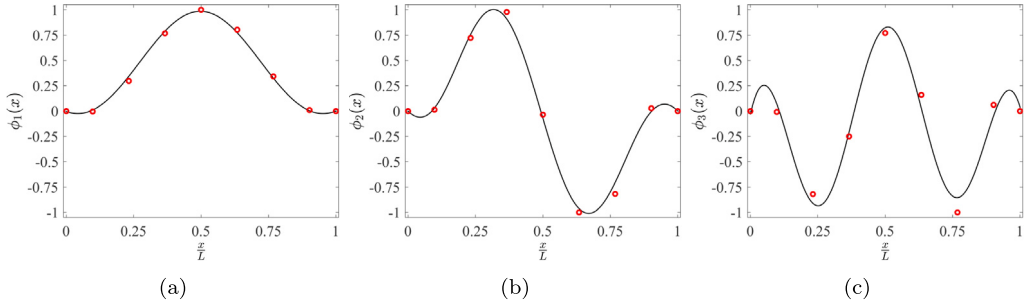

Fig. 8. Identified mode shapes of interest: (a) First ($R^2 = 1$), (b) second ($R^2 = 0.9992$) and (c) third ($R^2 = 0.9935$) vertical bending modes. Red dots: experimental data. Black line: Estimated curve. Lateral view of accelerometers a1 to a7 moving from south to north.

4.2. Simplified HSI formulations

One of the main hypotheses of Caprani's formulation [17] of the HSI framework is that the structural mode shapes will have negligible changes when pedestrians are considered. A representation of the coupled system in the modal domain is shown in Fig. 14; in this representation, the primary system is represented by the SDOF, with its corresponding modal mass, modal stiffness and associated damping of the considered mode n, and it is connected with the modulated pedestrians with their corresponding SDOF properties. Considering Caprani's formulation [17] in the frequency domain, under the hypothesis of a linear time-invariant system with non-moving pedestrians, it follows that

$$\begin{bmatrix} \mathbf{H}_{1,1} & \cdots & \mathbf{H}_{1,n} & \cdots & \mathbf{H}_{1,n+N_p} \\ \vdots & \ddots & \vdots & & \vdots \\ \mathbf{H}_{n,1} & \cdots & \mathbf{H}_{n,n} & \cdots & \mathbf{H}_{n,n+N_p} \\ \vdots & & \vdots & \ddots & \vdots \\ \mathbf{H}_{n+N_p,1} & \cdots & \mathbf{H}_{n+N_p,n} & \cdots & \mathbf{H}_{n+N_p,n+N_p} \end{bmatrix} \begin{Bmatrix} \mathbf{X}_1(\omega) \\ \vdots \\ \mathbf{X}_n(\omega) \\ \vdots \\ \mathbf{X}_{n+N_p}(\omega) \end{Bmatrix} = \begin{Bmatrix} \mathrm{P}_1(\omega) \\ \vdots \\ \mathrm{P}_n(\omega) \\ \vdots \\ 0 \end{Bmatrix}, \tag{12}$$

where the FRFs of each mode are found in the first n components of the diagonal of the FRF matrix and the off-diagonal terms represent the coupling terms of the system between structural modes and between

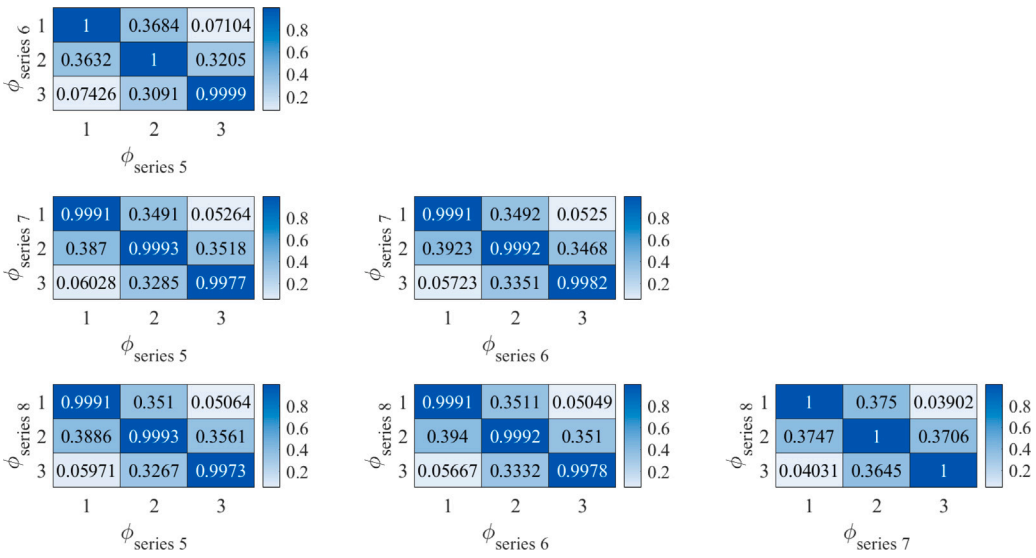

Fig. 9. MAC matrices of series 5 to 8 (with pedestrians and without pedestrians, layout C).

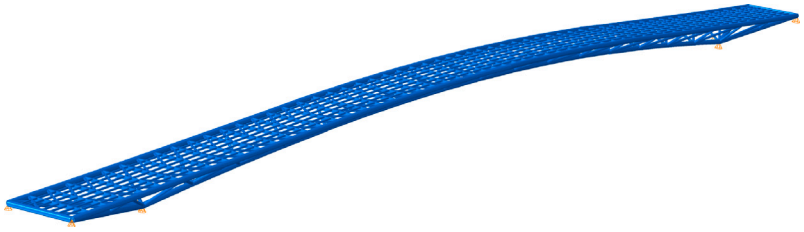

Fig. 10. FEM of the Folke Bernadotte Bridge.

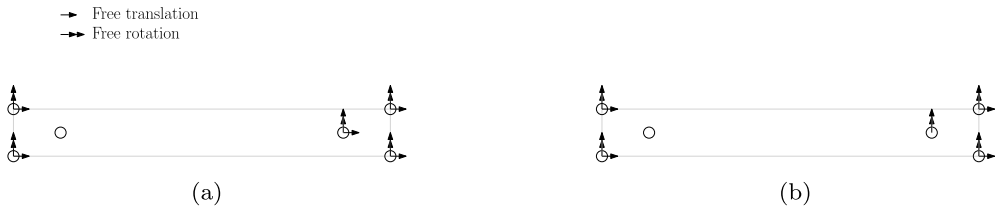

Fig. 11. (a) First boundary condition configuration and (b) second boundary condition configuration of the FEM of the Folke Bernadotte Bridge.

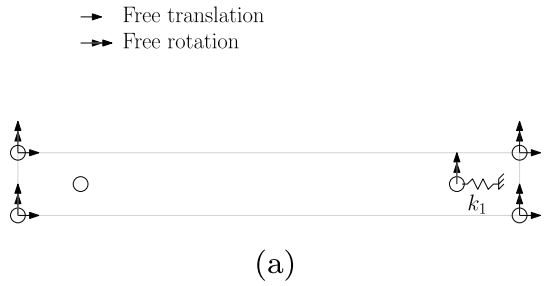

Fig. 12. Third boundary condition configuration, which considers a linear spring k_1 in the longitudinal direction of the FEM of the Folke Bernadotte Bridge.

structural modes and pedestrians. In order to validate Venuti's formulation [18] and the proposed closed-form expression for the FRF of the coupled pedestrian-bridge system in which a single mode is considered at a time, a quantification of the coupling terms of the more general Caprani's formulation [17] is performed in the following subsection, using as a reference the case study of the Folke Bernadotte Bridge.

4.2.1. Quantification of the direct and coupling terms

A theoretical evaluation of the HSI effect for the Folke Bernadotte Bridge was performed by computing the FRFs of the coupled system using Caprani's formulation [17]. The direct terms $\mathbf{H}_{1,1}$, $\mathbf{H}_{2,2}$ and $\mathbf{H}_{3,3}$ are evaluated by varying the natural frequency of the modelled pedestrians from 0 Hz to 10 Hz in the matrix formulation presented in Eq. (12). A damping of 40% was assumed for the pedestrians, and the reference natural frequencies and damping of the structural system for the theoretical analysis are ($f_1 = 1.69$ Hz; $\zeta_1 = 1.5\%$), ($f_2 = 3.02$ Hz; $\zeta_2 = 0.8\%$) and ($f_3 = 5.29$ Hz; $\zeta_3 = 0.8\%$). The FRFs at the measurement points x_j due to hammer hits at x_h are obtained as follows:

$$\hat{\mathbf{H}}_{x_j,x_\text{h}}(\omega) = \sum_{n=1}^{3} \phi_n(x_j)\phi_n(x_\text{h})\mathbf{H}_{n,n}(\omega). \tag{13}$$

The results of the theoretical evaluation are shown in Fig. 15. The influence of the HSI effect on the considered modes of vibration can be seen in the reduction of the magnitude of the FRFs; the natural frequency of the pedestrians falls within the region around the natural frequencies of the structural system, which are denoted by the three vertical red dashed lines. Fig. 15 also exposes the frequency shift of the coupled system; the natural frequency of the pedestrians falls within the range of the natural frequencies of the structural system.

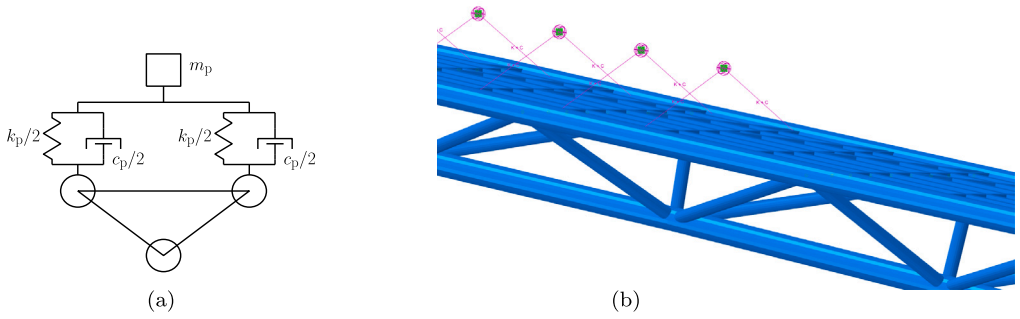

Fig. 13. (a) Schematic of the modelling approach of the SDOF representing the pedestrian system in the Abaqus FEM and (b) FEM of the coupled pedestrian bridge system in Abaqus.

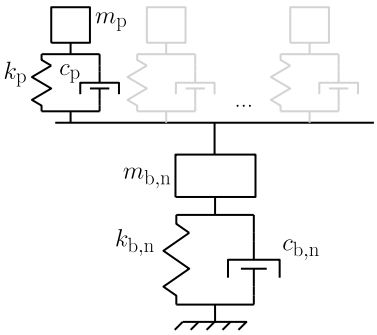

Fig. 14. Schematic of the coupled pedestrian-bridge system in the modal domain for one single structural mode.

From the theoretical results shown in Fig. 15, it is expected that there will be high levels of interaction between the pedestrians and the structure in the three considered vertical modes of vibration, such that the SMD model representing the pedestrians can be identified. To quantify the influence of the coupling between modes due to the presence of the pedestrians, the coupling terms $\mathbf{H}_{1,2}$, $\mathbf{H}_{2,3}$ and $\mathbf{H}_{1,3}$ of the matrix formulation presented in Eq. (12) based on Caprani's formulation [17] were computed by varying the natural frequency of the modelled pedestrians from 0 Hz to 10 Hz. The results are shown in Fig. 16. It can be seen that the magnitude of the coupling terms has a negligible influence since it is two to three orders of magnitude lower than the computed FRFs shown in Fig. 15. Therefore, it is sufficient to quantify the HSI effect by studying each mode of vibration separately and then adding their corresponding contributions.

4.3. Optimisation method

An automated FRF-based modal updating procedure [46] was implemented to address the inverse problem and to determine the material properties and the pedestrians' properties. The updating procedure is treated as a nonlinear optimisation problem that involves minimising the error between the theoretical FRFs $\mathbf{H}^{\mathrm{T}}(\omega)$ and the experimental FRFs $\mathbf{H}^{\mathrm{E}}(\omega)$ of the system. To evaluate the correlation between the theoretical and experimental FRFs, the frequency response assurance criterion (FRAC), which is sensitive to inconsistencies between the FRFs' shapes, and the frequency amplitude assurance criterion (FAAC), which is sensitive to the amplitude of the considered FRFs, were used. These two criteria vary between zero and one, where one indicates perfect correlation. For the specific accelerometer i, one obtains

$$\mathrm{FRAC}_i = \frac{\left\|(\mathbf{H}_i^{\mathrm{E}}(\omega))^H \mathbf{H}_i^{\mathrm{T}}(\omega)\right\|^2}{((\mathbf{H}_i^{\mathrm{E}}(\omega))^H \mathbf{H}_i^{\mathrm{E}}(\omega))((\mathbf{H}_i^{\mathrm{T}}(\omega))^H \mathbf{H}_i^{\mathrm{T}}(\omega))}, \tag{14}$$

Table 3
Initial, lower and upper values of the decision variables of the structural system.

		Initial value	Lower bound	Upper bound
Steel	E_s (GPa)	215	190	220
	ρ_s^a (kg/m^3)	8100	7800	8600
Elastic BC	k_1 (MN/m)	140	100	180
Damping	ζ_1 (–)	0.015	–	–
	ζ_2 (–)	0.008	–	–
	ζ_3 (–)	0.008	–	–

[a]Adjusted to account for the mass of the deck and railings in the FEM.

Table 4
Initial, lower and upper values of the decision variables of the reference pedestrian.

		Initial value	Lower bound	Upper bound
Frequency	f_p (Hz)	5.5	1	15
Damping	ζ_p (%)	35	20	70

$$\mathrm{FAAC}_i = \frac{2\left\|(\mathbf{H}_i^{\mathrm{E}}(\omega))^H \mathbf{H}_i^{\mathrm{T}}(\omega)\right\|}{((\mathbf{H}_i^{\mathrm{E}}(\omega))^H \mathbf{H}_i^{\mathrm{E}}(\omega)) + ((\mathbf{H}_i^{\mathrm{T}}(\omega))^H \mathbf{H}_i^{\mathrm{T}}(\omega))}. \tag{15}$$

The pattern search (PS) algorithm was used to minimise the objective function $f(\mathbf{X})$ (Eq. (16)), where p represents the number of decision variables in the decision vector $\mathbf{X} = (x_1, x_2, \ldots, x_p)$. The PS method was chosen due to its high convergence rate for a well-defined problem in which multiple local minima are not expected. To improve the optimisation procedure, all the decision variables were normalised from zero to one, which correspond to the lower bound and upper bound of the considered range, respectively. The PS is performed with an initial mesh size of 0.1, a mesh expansion factor of 1.95 and a mesh contraction factor of 0.75, and a complete poll strategy is used. The maximum number of iterations is set to 50 times p. The function tolerance and the mesh tolerance were set to 0.005 and 0.001, respectively. The objective function was computed for the different frequency ranges according to the consideration of the different structural modes. The analysis was performed on an Intel(R) Core (TM) i7-87000 CPU at 3.20 GHz (6 cores) with 32 GB of RAM. The initial values, as well as the lower and upper bounds, of the properties of the bridge system are shown in Table 3. The damping ratio of the considered modes is fixed for both the FEM and the modal model. The initial values, as well as the lower and upper bounds, of the properties of the reference pedestrian are shown in Table 4.

$$f(\mathbf{X}) = \sum_{i=1}^{N} \left\|\mathrm{FRAC}_i(\mathbf{X}) - 1\right\| + \left\|\mathrm{FAAC}_i(\mathbf{X}) - 1\right\| + \left\|\mathrm{FRAC}_i(\mathbf{X}) - 1\right\|^2 + \left\|\mathrm{FAAC}_i(\mathbf{X}) - 1\right\|^2. \tag{16}$$

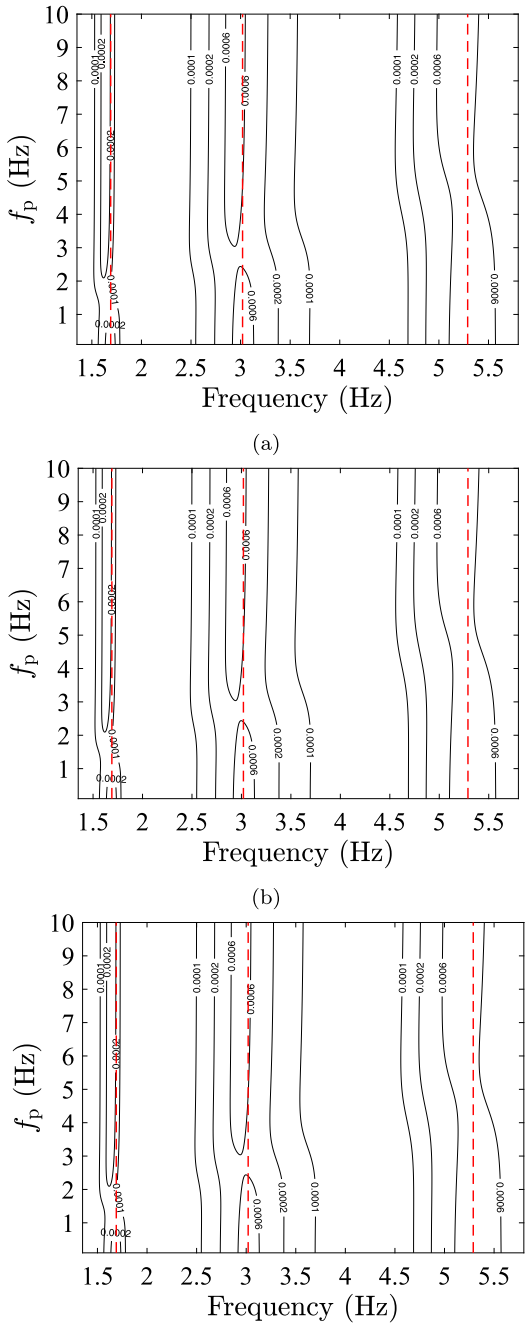

Fig. 15. Theoretical magnitude of the FRFs of the coupled pedestrian-bridge system as a function of the natural frequency of the pedestrians at (a) x = 22.5 m, (b) x = 35.5 m and (c) x = 48.5 m in terms of the layout of the line of accelerometers shown in Fig. 5. The red dashed (- -) lines indicate the natural frequencies of the empty bridge.

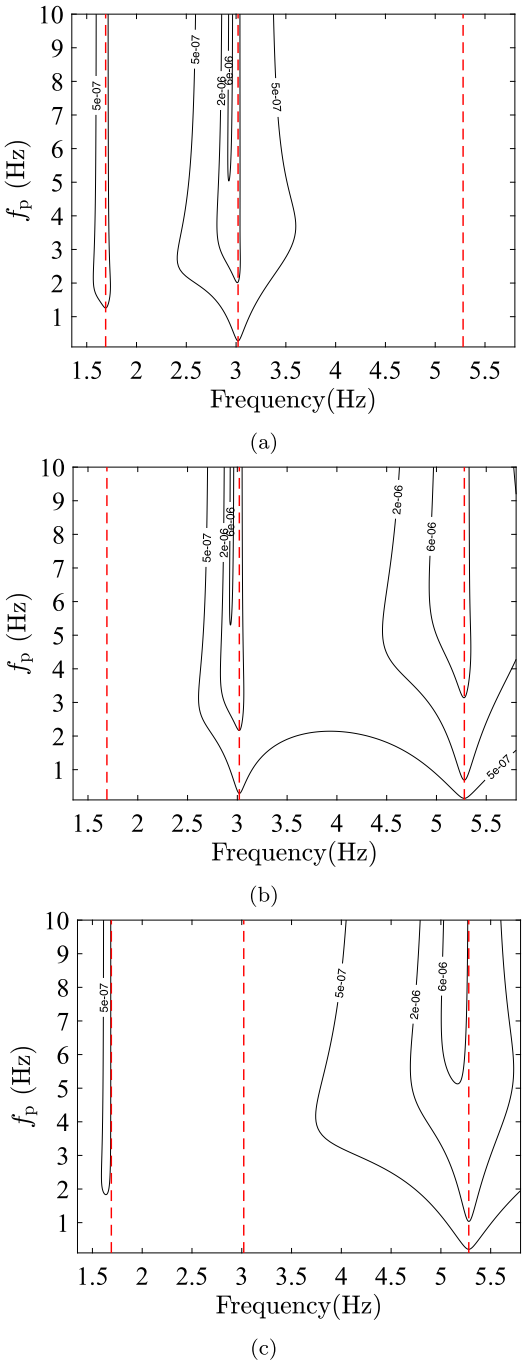

Fig. 16. Quantification of the magnitude of the coupling terms of Caprani's formulation as a function of the natural frequency of the pedestrians f_p: (a) accelerance FRFs $\mathbf{H}_{1,2}$, (b) accelerance FRFs $\mathbf{H}_{2,3}$ and (c) accelerance FRFs $\mathbf{H}_{1,3}$. The red dashed (- -) lines indicate the natural frequencies of the empty bridge.

5. Results and discussion

In this section of the work, the results of the updated FEM, the updated simplified models, i.e. Caprani's HSI formulation (referred to as the full HSI model), and the closed-form expression of the HSI problem are compared to the experimental results.

5.1. Bridge system

The updated parameters of the FEM are shown in Table 5. The parameters of the modal model that were updated using the experimentally fitted modes are shown in Table 6. Negligible differences in the natural frequencies between the models are found. The total weight of the adjusted model is 90.3 tons. The linear mass density assumed for the modal model is 930 kg/m. The updated FRFs obtained from the FEM and the modal model are presented in Fig. 17. Good agreement between the FRFs of both models was obtained: the peaks and shapes of the FRFs of both models coincided. The partial mismatch in the peak of the first mode of vibration can be explained by the influence of the first lateral mode of the structural system, which has a vertical component at the centre of the bridge that is shown in Fig. 17c. Additionally, in Fig. 17c, a small peak around 3.50 Hz produced by a torsional mode can be seen. The contribution of this mode was not completely examined in

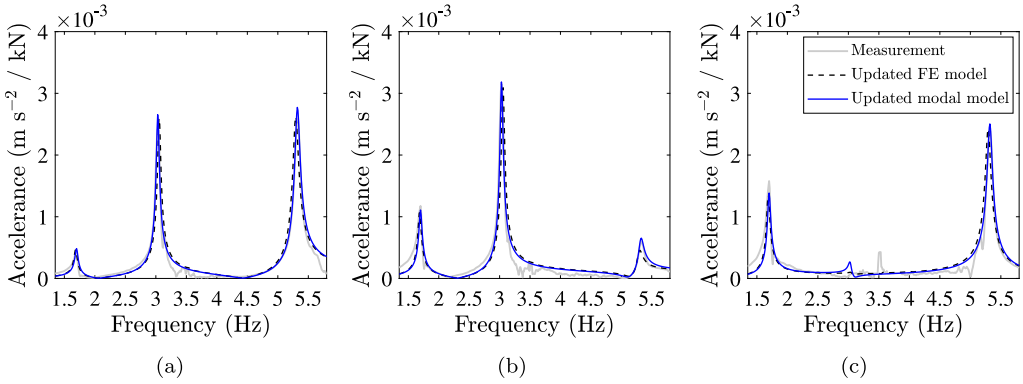

Fig. 17. Updated accelerance FRFs of the FEM (dashed lines (- -)) and the modal model (blue solid lines (-)) and the measurement FRFs (grey solid lines (-)) at (a) $x = 22.5$ m, (b) $x = 35.5$ m and (c) $x = 48.5$ m. Panels (a), (b) and (c) correspond to the layout of the line of accelerometers shown in Fig. 5. (For interpretation of the references to colour in this figure legend, the reader is referred to the web version of this article.)

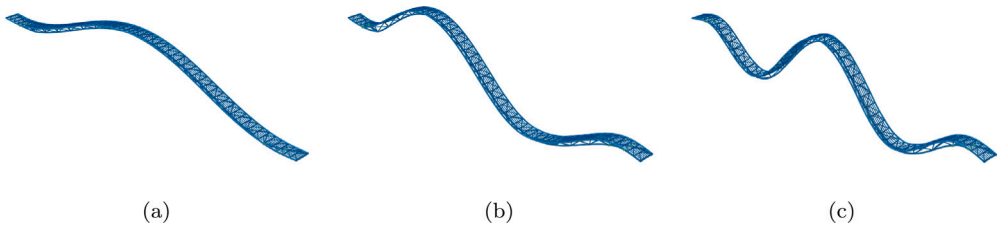

Fig. 18. Mode shapes from the FEM of the Folke Bernadotte Bridge.

Table 5
Updated variables of the structural system based on the FEM.

		Updated value
Steel	E_s (GPa)	210.5
	ρ_s^a (kg/m^3)	8395
Elastic BC	k_1 (MN/m)	152.2
Modes	f_1 (Hz)	1.70
	f_2 (Hz)	3.03
	f_3 (Hz)	5.32

Table 6
Updated variables of the structural system based on the modal model and the experimentally fitted modes.

		Updated value
Modes	f_1 (Hz)	1.69
	f_2 (Hz)	3.01
	f_3 (Hz)	5.28

the averaging of the two opposing accelerometers. The three considered modes of vibrations of the FEM are shown in Fig. 18. Finally, Fig. 19 shows the MAC matrices computed between the experimental curves and the FEM for the two different boundary condition configurations. Negligible differences were found for the calibrated FEM. Figs. 19(a) and 19(b) prove the reliability of the FEM (both with fixed–fixed (FF) ends and fixed–movable (FM) ends, in the same order). Fig. 19(c) compares the two configurations considered for the FE model, showing overall the strong similarity of the mode shapes resulting from the numerical simulations. Finally, the updated FEM and the updated modal model can be used to calibrate the human SMD model, as well as to quantify the HSI effect. To evaluate the modelling approach of adjusting the steel density instead of modelling the timber, the spruce pieces conforming the deck were considered in a separated model. The differences in mass were less than 1% and the differences in frequency of the first, second and third mode were 1.19%, 0.66% and 0.57%, respectively. Hence, the model in which only the steel is used was further verified.

Table 7
Updated values of the reference pedestrian, taking into account all the considered modes (1.35–6.00 Hz).

		FEM	Full HSI model	Closed-form
Frequency	f_p (Hz)	5.01	5.00	5.00
Damping	ζ_p (%)	37.13	44.09	42.85

Table 8
Updated values of the reference pedestrian, taking into account the second and third modes (2.30–6.00 Hz).

		FEM	Full HSI model	Closed-form
Frequency	f_p (Hz)	5.01	5.08	5.00
Damping	ζ_p (%)	35.57	40.62	41.35

5.2. Human–structure system

Once the modal model and the FEM were updated, they were used as a reference to calibrate the human SMD model. The modal mass ratios of the coupled pedestrian-bridge system ($\sum_{r=1}^{35} m_{p,r}\phi_{r,n}^2/m_{b,n}$) for the first, second and third modes are 5.58%, 4.90% and 4.15%, respectively. Moreover, three different frequency bands were considered to quantify the influence of the different structural modes. In the first case, all three structural modes were taken into account by considering a frequency band from 1.35 Hz to 6.00 Hz. In the second case, the second and third structural modes were taken into account by considering a frequency band from 2.30 Hz to 6.00 Hz. In the third case, only the third structural mode was taken into account by considering a frequency band from 4.00 Hz to 6.00 Hz. The results of the aforementioned cases of the updated SMD model are shown in Tables 7–9, respectively.

It can be seen that there is consistency in the results among the three considered models and the three considered frequency bands regarding the natural frequency of the pedestrians; the results indicate a value

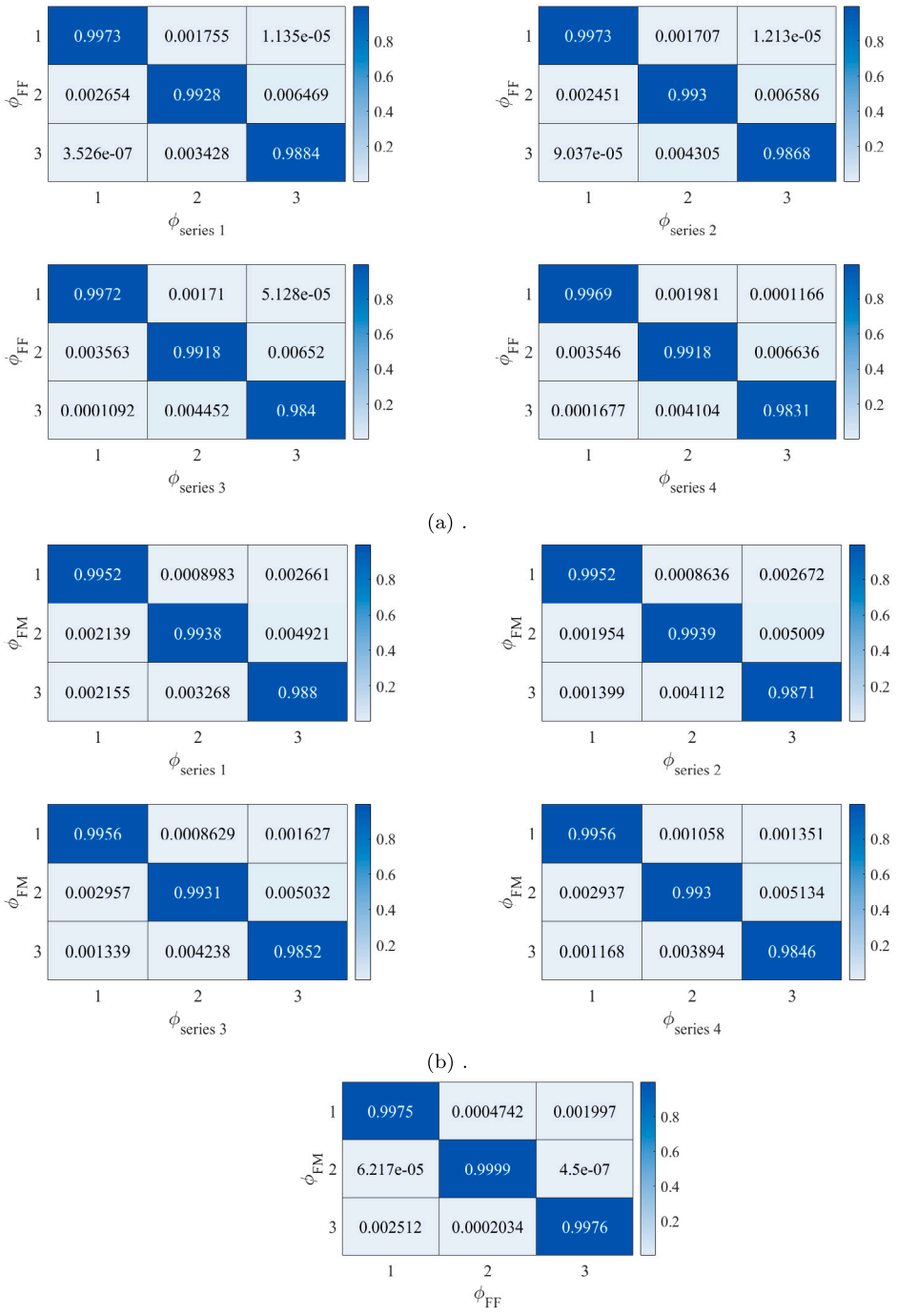

Fig. 19. MAC matrices of the experimental findings (without pedestrians, layout A) vs. (a) the FEM with FF boundary conditions and (b) the FEM with FM boundary conditions. (c) MAC values between the two numerical models.

Table 9
Updated values of the reference pedestrian, taking into account the third mode (4.00–6.00 Hz).

		FEM	Full HSI model	Closed-form
Frequency	f_p (Hz)	5.15	5.26	5.20
Damping	ζ_p (%)	39.46	39.20	38.50

around 5 Hz. This is a result consistent with the values for the human SMD models found in [47–50].

In the case of the damping associated with the pedestrians, in both the first case and the second case, the updated FEM led to lower values with respect to both the full HSI model and the closed-form solution. In the first case, in which all the structural modes are taken into account, the difference in damping between the FEM and full HSI model was 6.96%. The difference in damping between the FEM and the closed-form solution was 5.72%. In the second case, in which the second and third structural modes are taken into account, the difference in damping between the FEM and full HSI model was 5.05%. The difference in damping between the FEM and the closed-form solution was 5.78%. In the third case, in which only the third structural mode

is considered, the difference in damping between the FEM and full HSI model was 0.26%. The difference in damping between the FEM and the closed-form solution was 0.96%. The differences found indicate the difficulties involved in quantifying the human SMD model. The results suggest that a probabilistic approach may be more suitable for characterising the human model.

A comparison among the FRFs obtained from the updated FEM, the full HSI model and the closed-form solution for the first case, in which all structural modes are taken into account, is shown in Fig. 20. It can be seen that there is great agreement between the FEM, the full HSI model and the closed-form solution with respect to the measurements for the second mode and the third mode. However, there is disagreement for the first mode in terms of both the amplitude and frequency. Considering the agreement of the three models, the authors make the following suggestions:

- The human SMD model consisting of one SDOF system is not able to replicate the influence of the HSI effect for all of the considered frequency band, suggesting that a more complete model that uses at least two SDOF systems to represent the pedestrians may lead to better results.
- The stiffness of the considered elastic boundary conditions changed due to the presence of pedestrians. As a result, it would be possible to again update the stiffness value of the FEM to increase the agreement between the FEM and the measurements. However, the authors consider the experimental results as a case study that shows the importance of not only the uncertainties related to the human models but also the uncertainties associated with the load case scenario [51] and the structural system itself [52]. Indeed, the damping ratio of the structural system is inherently random and difficult to quantify [53], and the estimate of the natural frequencies is influenced by uncertainties in the numerical models [54], the environmental conditions of the particular system [55], the load case scenario and boundary conditions, as shown by the measurements made while there were pedestrians on the Folke Bernadotte Bridge [51].

All the aforementioned uncertainties are present in the serviceability assessment, evaluation and identification of the structural response [51,56–58]. Additionally, in the context of the serviceability limit state, even the variability of the perception of the vibration levels of a considered system should be taken into account [59,60].

Furthermore, the perfectly modulated attached mass model, i.e. the model that assumes that the pedestrians are perfectly attached to the system, is considered, and the changes in the natural frequency of the system for the first mode of vibration are evaluated. This is done by considering two systems consisting of an SDOF in which the stiffness has a constant value and the natural frequency and the mass change. From the experiment, the structure without humans has a first natural frequency of 1.70 Hz. Considering humans, it has a first natural frequency of 1.46 Hz. This leads to a modal mass ratio of 16.44%. Conversely, the modal mass ratio for the first mode was equal to 5.58%. Hence, it is demonstrated that the mismatch cannot be explained by the perfectly modulated attached model, suggesting that either changes in the boundary conditions due to the load case (experimental campaign with standing pedestrians) occurred or that a more complete human model is needed.

The three modes of vibration of the FEM, considering the pedestrians, are shown in Fig. 23. The MAC values computed between these modes and the corresponding experimental measurements (series 7 and 8) are reported in Fig. 21.

Additionally, Figs. 22(a) and 22(b) show, respectively, the MAC values of the pedestrian-loaded FEM vs. the unloaded experimental mode shapes. Specifically, Fig. 22(a) refers to series 1 and 2 (layout A), while Fig. 22(b) refers to series 3 and 4 (layout B). These results clearly highlight that the differences between the human-loaded FE model and unloaded mode shapes are small in absolute terms (the MAC values on the main diagonal never fall below 0.97) but non-negligible in relative terms, as the MAC values of Fig. 21 were all higher than 0.99. Nevertheless, one should consider that the changes induced by the pedestrians in the mode shapes are limited.

Table 10
Range of values considered for the parametric analysis.

Parameter	Solution	Range
f_p (Hz)	5.00	[4,6]
ζ_p (%)	0.4285	[0.20,0.70]
f_1 (Hz)	1.69	[1.60,1.80]
f_2 (Hz)	3.01	[2.90,3.10]
f_3 (Hz)	5.28	[5.18,5.38]

Taking $f_p = 5$ Hz and the calibrated values of the empty structure from Table 6, the tuning parameters, i.e. the frequency ratios between the natural frequencies of the first, second and third modes, are 2.96, 1.65 and 0.94, respectively. It can be seen in Fig. 23 and in [5] that the level interaction between the two subsystems is defined by the ratio between the natural frequency of the reference pedestrian and the natural frequency of the considered mode such that (i) for low-frequency ratios ($\omega_p/\omega_b < 0.5$), the crowd and the supporting structure are decoupled, (ii) for intermediate-frequency ratios ($0.5 < \omega_p/\omega_b < 1.5$), a high level of interaction is developed, increasing the effective damping of the system and shifting the natural frequency of the coupled system, and (iii) for high-frequency ratios ($\omega_p/\omega_b > 1.5$), the crowd is stiffer than the supporting structure, and hence it acts as an additional mass. This is shown in Fig. 23c for intermediate-frequency ratios; the SMD models representing the pedestrians are nearly tuned to the third natural frequency of the bridge, dissipating most of the energy, increasing the damping and changing the natural frequency of the coupled system, i.e. the HSI effect. It can be seen that this effect is gradually reduced in Fig. 23b and in Fig. 23a, which correspond to high-frequency ratios for which the SMD models representing the pedestrians follow the supporting system as attached masses. Finally, in order to verify the results, a sensitivity analysis is performed in the vicinity of the solution found for the human SMD model (f_p, ζ_p) in the next subsection.

5.3. Sensitivity analysis

In this subsection, a sensitivity analysis of the determined solution is presented for the human SMD model (f_p, ζ_p) and the reference system (f_1, f_2, f_3) based on the closed-form solution. The sensitivity analysis is performed using the closed-form solution, given the validity of the results, considering the frequency range of 1.35 Hz to 6.00 Hz (the three structural modes). The objective function (Eq. (16)) is sampled considering the range of parameters shown in Table 10.

The results of the sensitivity analysis of the case study are shown in Fig. 24.

The sensitivity analysis results are discussed in a top-down, left-to-right order:

- ζ_p vs. f_p: This plot shows that the objective function around the reference solution (red circle) of the human SMD model behaves as a convex valley in which variations of the pedestrian parameters will not significantly change the objective function. Variations of the natural frequency of the pedestrian $\Delta f_p = 4.7 - 5.4 = 0.7$ Hz, in combination with variations of the damping of the pedestrian $\Delta\zeta_p = 0.55 - 0.35 = 0.2$, will produce similar values of the objective function (<5.2). This exposes the difficulties involved in defining the human SMD model. However, these ranges of values for f_p and ζ_p are in agreement with [47–50]. The location of the reference solution with respect to the evaluated surface indicates the quality of the solution.

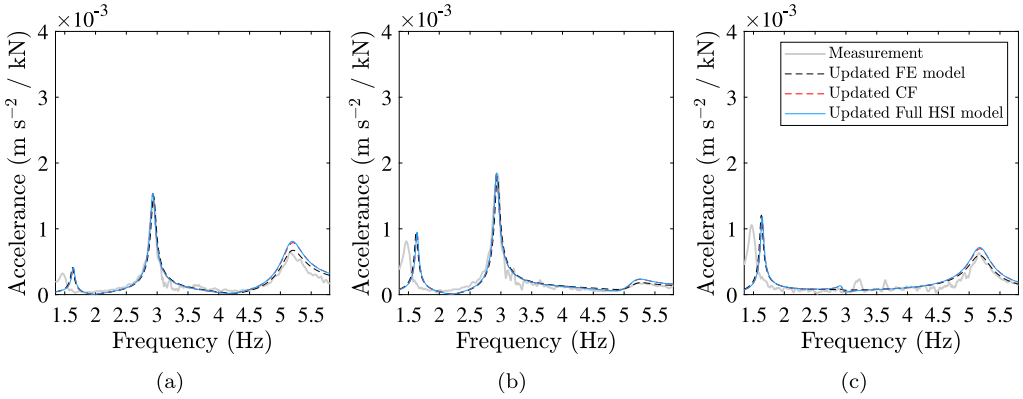

Fig. 20. Updated accelerance FRFs of the FEM (black dashed lines (- -)), the full HSI model (Caprani's formulation) (blue solid lines (-)) and the closed-form solution (dashed red lines (- -)) and the measurement FRFs (grey solid lines (-)) at (a) $x = 22.5$ m, (b) $x = 35.5$ m and (c) $x = 48.5$ m. Panels (a), (b) and (c) correspond to the layout of the line of accelerometers shown in Fig. 5. (For interpretation of the references to colour in this figure legend, the reader is referred to the web version of this article.)

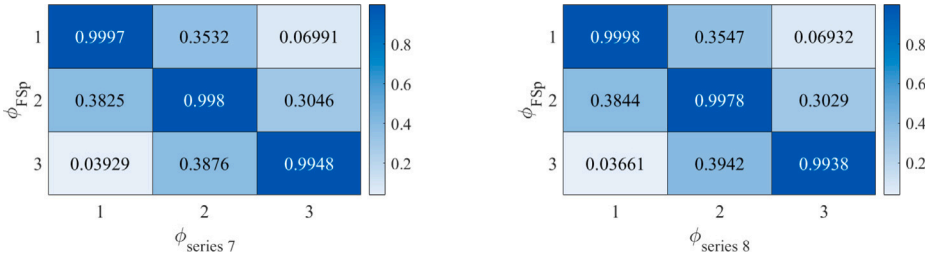

Fig. 21. MAC matrices of the FEM with fixed-spring boundary conditions and pedestrians vs. the experimental findings (with pedestrians, layout C).

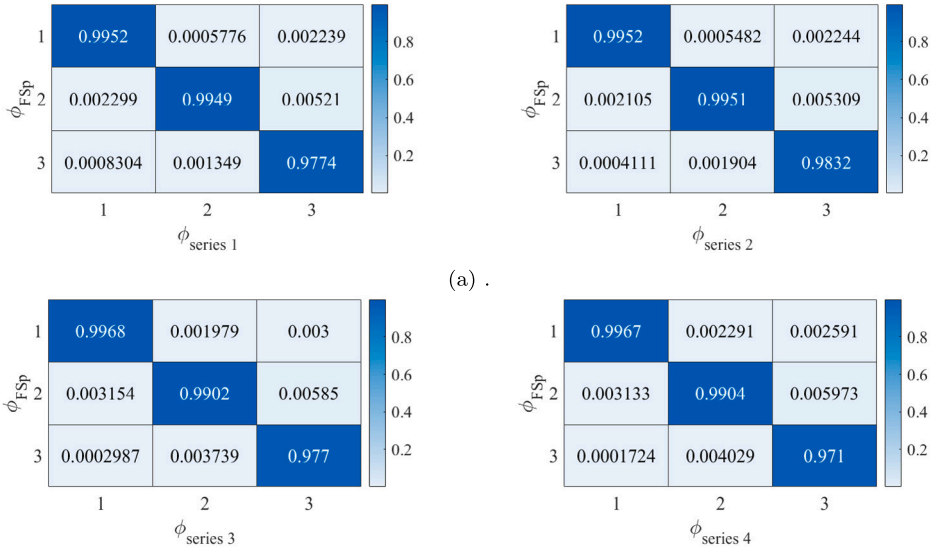

Fig. 22. MAC matrices of the FEM with fixed-spring boundary conditions and pedestrians vs. (a) without pedestrians — layout A, and (b) without pedestrians — layout B.

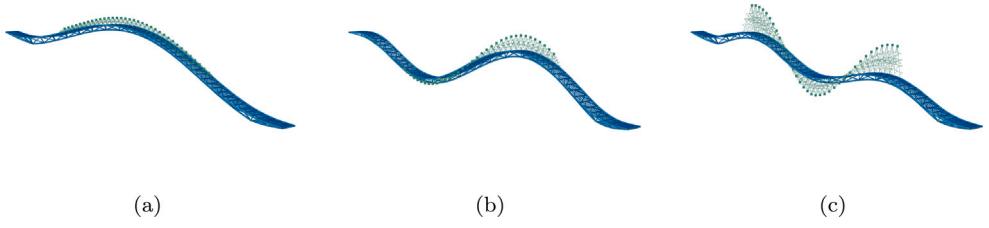

Fig. 23. Mode shapes of the coupled pedestrian-bridge system of the FEM: (a) First vertical mode of vibration, (b) second vertical mode of vibration and (c) third vertical mode of vibration.

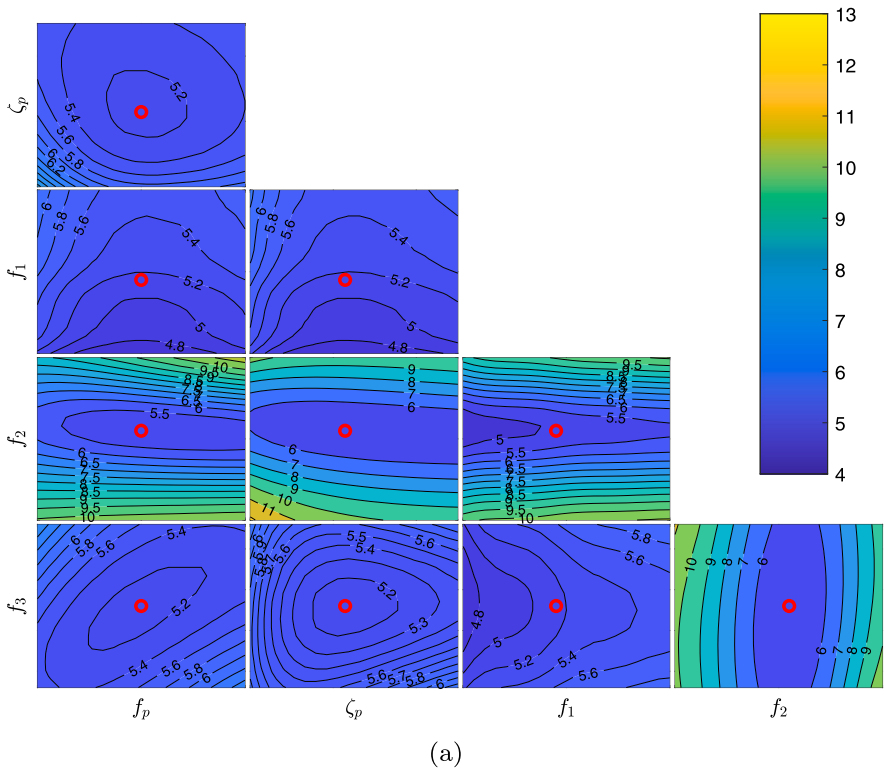

(a)

Fig. 24. Sensitivity analysis of the determined solution. The red circles denote the reference solution.

- f_1 vs. f_p: This plot shows the mismatch of the first mode of vibration and that the reference value of the natural frequency of the pedestrian f_p is at the centre of the descending surface, indicating the high quality of the solution that minimises the objective function.
- f_2 vs. f_p: This plot shows that there is a combination of the considered parameters that can give similar values of the objective function (mostly because of variations of the natural frequency of the pedestrian). These results show the importance of characterising the supporting structure properly and the difficulties involved in defining the human SMD model. The location of the reference solution with respect to the evaluated surface indicates the quality of the solution. The results reflect the importance of the second mode of vibration in the modal updating scheme that was adopted, given the variations of the objective function on the vertical axis.
- f_3 vs. f_p: This plot shows that there is a region in which a combination of the considered parameters can give similar values of the objective function (<5.2). That is, variations of the natural frequency of the pedestrian $\Delta p = 5.5-4.5 = 1.0$ Hz, in combination with variations of the third natural frequency of the empty bridge $\Delta f_3 = 5.3 - 5.2 = 0.1$ Hz, will produce similar values of the objective function. This is consistent with the differences found between the calibrated FEM and the closed-form solution model shown in Tables 7–9. The diagonal behaviour of the surface of the objective function indicates the predominately high level of the HSI effect between the third structural mode and the pedestrians. The location of the reference solution with respect to the evaluated surface indicates the quality of the solution that minimises the objective function.
- f_1 vs. ζ_p: This plot shows the mismatch of the first mode of vibration and that the reference value of the damping of the pedestrian ζ_p is at the centre of the valley, indicating the high quality of the solution that minimises the objective function, i.e. in the direction of the steepest descent.
- f_2 vs. ζ_p: This plot shows that there is a region in which a combination of the considered parameters can give similar values of the objective function (mostly because of variations of the damping of the pedestrian). These results show the importance of characterising the supporting structure properly and the difficulties involved in defining the damping of the human SMD model. The location with respect to the evaluated surface of the reference solution that minimises the objective function indicates the quality of the solution.
- f_3 vs. ζ_p: This plot suggests that variations of the third natural frequency of the empty structure, i.e. $\Delta f_3 = 5.3-5.24 = 0.06$ Hz, with respect to variations of the damping of the pedestrian, i.e. $\Delta\zeta_p = 0.55 - 0.35 = 0.2$, can give similar values of the objective function around the determined solution (red circle). This exposes the difficulties involved in defining the damping parameter associated with the human SMD model and the importance of properly defining the modal parameters of the supporting structure. The location of the reference solution with respect to the evaluated surface indicates the quality of the solution.
- f_2 vs. f_1: This plot shows that the second natural frequency f_2 is very well defined and the mismatch of the first mode of vibration.
- f_3 vs. f_1: This plot shows that the third natural frequency f_3 is defined within the considered range and the mismatch of the first mode of vibration.
- f_3 vs. f_2: This plot shows that the third natural frequency f_3 has variations within the considered range with respect to the second natural frequency f_2. This is explained by the HSI effect: the FRFs concerning the third mode of vibration of the coupled system are highly damped due to the tuning of the pedestrians (ω_b/ω_b). The location with respect to the evaluated surface of the reference solution that minimises the objective function indicates the quality of the determined solution.

The previous analysis shows how difficult it is to characterise the human SMD model and the need to take the system variability, from

both the human SMD model perspective and the supporting structure perspective, into account by means of a reliability-based framework [61] or using interval analysis, as in [62]. For other frequency ranges in which the second and third structural modes are considered and for the case in which only the third mode is considered, the corresponding surfaces of the evaluated objective functions are narrower and well defined.

6. Conclusions

An analytical expression for the FRF of the coupled pedestrian-bridge system was presented. The analytical expression was validated by the presented case study on the Folke Bernadotte Bridge. Great agreement was obtained between the theoretical and experimental FRFs. The quantification of the coupling terms between the structural modes in the HSI formulation allowed these terms to be evaluated, and it was found that they had a negligible influence. The determined analytical expression was proven to be suitable for the case in which one single structural mode is taken into account, and it was validated against the calibrated FEM and the considered HSI formulations. The partial mismatch between the theoretical and experimental FRFs suggests the importance of considering the uncertainties of the system, its boundary conditions and the limitations of the considered human model. The properties of the pedestrian SMD model were identified, and good agreement with the properties reported in the literature was obtained. Finally, by preforming a sensitivity analysis of the determined solution, it was demonstrated that, in this case, an optimisation scheme is not the best approach for characterising the human model. A probabilistic approach or a framework based on interval analysis that can be used to define the human SMD properties are more suitable strategies for defining a human model with reliable values of the mechanical properties. The sensitivity analysis validates the closed-form expression of the FRF for the coupled pedestrian-bridge system.

Declaration of competing interest

The authors declare that they have no known competing financial interests or personal relationships that could have appeared to influence the work reported in this paper.

Acknowledgement

This work is part of the research developed by the first author within the framework of the BBT project 2020-023, which is a continuation of the BBT project 2017-004 supported by Trafikverket.

Appendix. Fitted mode shapes

$$\begin{aligned}
\phi_1(x/L) &= 0.5292\sin(0.0127(x/L)+0.9588)\\
&\quad +0.4757\sin(0.07355(x/L)+4.306).\\
\phi_2(x/L) &= 0.6894\sin(0.05439(x/L)+0.5589)\\
&\quad +0.7176\sin(0.1236*(x/L)-2.812)\\
&\quad +0.2181\sin(0.1426(x/L)-0.6552).\\
\phi_3(x/L) &= -2.5756-1.215\cos(3.6608(x/L))+4.1696\sin(3.6608(x/L))\\
&\quad +2.3447\cos(7.3216(x/L))+1.4501\sin(7.3216(x/L))\\
&\quad +1.4112\cos(10.9823(x/L))-1.2107\sin(10.9823(x/L)).
\end{aligned} \tag{A.1}$$

References

[1] He L, Castoro C, Aloisio A, Zhang Z, Marano GC, Gregori A, Deng C, Briseghella B. Dynamic assessment, FE modelling and parametric updating of a butterfly-arch stress-ribbon pedestrian bridge. Struct Infrastruct Eng 2022;18(7):1064–75. http://dx.doi.org/10.1080/15732479.2021.1995444.
[2] Quqa S, Giordano PF, Limongelli MP. Shared micromobility-driven modal identification of urban bridges. Autom Constr 2022;134:104048. http://dx.doi.org/10.1016/j.autcon.2021.104048.
[3] Ricciardelli F, Demartino C. Design of footbridges against pedestrian-induced vibrations. J Bridge Eng 2016;21(8):C4015003.
[4] Shahabpoor E, Pavic A, Racic V. Structural vibration serviceability: New design framework featuring human-structure interaction. Eng Struct 2017;136:295–311.
[5] Van Nimmen K, Lombaert G, De Roeck G, Van den Broeck P. The impact of vertical human-structure interaction on the response of footbridges to pedestrian excitation. J Sound Vib 2017;402:104–21. http://dx.doi.org/10.1016/j.jsv.2017.05.017.
[6] Sétra Faoce. Technical guide. Footbridges. Assessment of vibrational behaviour of footbridges under pedestrian loading. 2006.
[7] FIB. Bulletin 32: Guidelines for the design of footbridges. Fed Int Beton 2005.
[8] Steel C, Part CB. 2: Specification for loads; Appendix C: Vibration serviceability requirements for foot and cycle track bridges, BS 5400. UK, London: British Standards Association; 1978.
[9] ISO. 10137: Bases for design of structures - Serviceability of buildings and walkways against vibrations. International Organization for Standardization (ISO); 2007.
[10] EN I. Eurocode 5: Design of timber structures—Part 2: Bridges. Brussels: The European Committee for Standardisation; 2004.
[11] Geißler K. Steel bridges. Conceptual and structural design of steel and steel-concrete composite bridges. Stahlbau 2014;83(9):682.
[12] Heinemeyer C, Butz C, Keil A, Schlaich M, Goldack A, Trometer S, Lukic M, Chabrolin B, Lemaire A, Martin P-O, et al. Design of Leightweight footbridges for human induced vibrations. 2009.
[13] Caetano E, Cunha A, Hoorpah W, Raoul J. Footbridge vibration design. London: CRC Press; 2014, http://dx.doi.org/10.1201/9781482266511.
[14] Willford MR, Young P, CEng M. A design guide for footfall induced vibration of structures. Concrete Society for The Concrete Centre; 2006.
[15] Sachse R, Pavic A, Reynolds P. Parametric study of modal properties of damped two-degree-of-freedom crowd–structure dynamic systems. J Sound Vib 2004;274(3):461–80.
[16] Shahabpoor E, Pavic A, Racic V. Identification of mass–spring–damper model of walking humans. Structures 2016;5:233–46. http://dx.doi.org/10.1016/j.istruc.2015.12.001.
[17] Caprani CC, Ahmadi E. Formulation of human–structure interaction system models for vertical vibration. J Sound Vib 2016;377:346–67. http://dx.doi.org/10.1016/j.jsv.2016.05.015.
[18] Venuti F, Racic V, Corbetta A. Modelling framework for dynamic interaction between multiple pedestrians and vertical vibrations of footbridges. J Sound Vib 2016;379:245–63. http://dx.doi.org/10.1016/j.jsv.2016.05.047.
[19] Zhang M, Georgakis CT, Chen J. Biomechanically excited SMD model of a walking pedestrian. J Bridge Eng 2016;21(8):C4016003. http://dx.doi.org/10.1061/(ASCE)BE.1943-5592.0000910.
[20] Ahmadi E, Caprani C, Živanović S, Evans N, Heidarpour A. A framework for quantification of human-structure interaction in vertical direction. J Sound Vib 2018;432:351–72. http://dx.doi.org/10.1016/j.jsv.2018.06.054.
[21] Busca G, Cappellini A, Manzoni S, Tarabini M, Vanali M. Quantification of changes in modal parameters due to the presence of passive people on a slender structure. J Sound Vib 2014;333(21):5641–52. http://dx.doi.org/10.1016/j.jsv.2014.06.003.
[22] Qin J, Law S, Yang Q, Yang N. Pedestrian–bridge dynamic interaction, including human participation. J Sound Vib 2013;332(4):1107–24. http://dx.doi.org/10.1016/j.jsv.2012.09.021.
[23] Wei X, Živanović S. Frequency response function-based explicit framework for dynamic identification in human-structure systems. J Sound Vib 2018;422:453–70. http://dx.doi.org/10.1016/j.jsv.2018.02.015.
[24] Fanning P, Archbold P, Pavic A. A novel interactive pedestrian load model for flexible footbridges. In: Proceedings of the 2005 Society for Experimental Mechanics Annual Conference on Experimental and Applied Mechanics, Portland, Oregon, June. 2005, p. 7–9.
[25] da Silva FT, Brito HMBF, Pimentel RL. Modeling of crowd load in vertical direction using biodynamic model for pedestrians crossing footbridges. Can J Civil Eng 2013;40(12):1196–204. http://dx.doi.org/10.1139/cjce-2011-0587.
[26] Toso MA, Gomes HM. A coupled biodynamic model for crowd-footbridge interaction. Eng Struct 2018;177:47–60. http://dx.doi.org/10.1016/j.engstruct.2018.09.033.
[27] Dang HV, Živanović S. Modelling pedestrian interaction with perceptibly vibrating footbridges. FME Trans 2013;41(4):271–8.
[28] Van Nimmen K, Lombaert G, De Roeck G, Van den Broeck P. Vibration serviceability of footbridges: Evaluation of the current codes of practice. Eng Struct 2014;59:448–61.

[29] Ricciardelli F, Demartino C. Design of footbridges against pedestrian-induced vibrations. J Bridge Eng 2016;21(8).
[30] Jiménez-Alonso JF. Recent advances in the serviceability assessment of footbridges under pedestrian-induced vibrations. IntechOpen; 2018.
[31] Dong C-Z, Bas S, Catbas FN. Investigation of vibration serviceability of a footbridge using computer vision-based methods. Eng Struct 2020;224:111224.
[32] Venuti F, Tubino F. Human-induced loading and dynamic response of footbridges in the vertical direction due to restricted pedestrian traffic. Struct Infrastruct Eng 2021;17(10):1431–45.
[33] Van Nimmen K, Van Hauwermeiren J, Van den Broeck P. Eeklo footbridge: Benchmark dataset on pedestrian-induced vibrations. J Bridge Eng 2021;26(7).
[34] Van Nimmen K, Pavic A, Van den Broeck P. A simplified method to account for vertical human-structure interaction. Structures 2021;32:2004–19. http://dx.doi.org/10.1016/j.istruc.2021.03.090.
[35] Ahmadi E, Caprani CC, Heidarpour A. An equivalent moving force model for consideration of human-structure interaction. Appl Math Model 2017;51:526–45. http://dx.doi.org/10.1016/j.apm.2017.06.042.
[36] Maraveas C, Fasoulakis Z, Tsavdaridis K. A review of human induced vibrations on footbridges. Science Publications; 2015.
[37] Colmenares D, Andersson A, Karoumi R. Closed-form solution for mode superposition analysis of continuous beams on flexible supports under moving harmonic loads. J Sound Vib 2022;520:116587. http://dx.doi.org/10.1016/j.jsv.2021.116587.
[38] Johansson C, Pacoste C, Karoumi R. Closed-form solution for the mode superposition analysis of the vibration in multi-span beam bridges caused by concentrated moving loads. Comput Struct 2013;119:85–94. http://dx.doi.org/10.1016/j.compstruc.2013.01.003.
[39] Martínez-Castro A, Museros P, Castillo-Linares A. Semi-analytic solution in the time domain for non-uniform multi-span Bernoulli–Euler beams traversed by moving loads. J Sound Vib 2006;294(1):278–97. http://dx.doi.org/10.1016/j.jsv.2005.11.009.
[40] Museros P, Moliner E, Martínez-Rodrigo M. Free vibrations of simply-supported beam bridges under moving loads: Maximum resonance, cancellation and resonant vertical acceleration. J Sound Vib 2013;332(2):326–45. http://dx.doi.org/10.1016/j.jsv.2012.08.008.
[41] Bulajić B, Todorovska MI, Manic MI, Trifunac MD. Structural health monitoring study of the ZOIL building using earthquake records. Soil Dyn Earthq Eng 2020;133:106105. http://dx.doi.org/10.1016/j.soildyn.2020.106105.
[42] Civera M, Calamai G, Zanotti Fragonara L. System identification via fast relaxed vector fitting for the structural health monitoring of masonry bridges. Structures 2021;30:277–93. http://dx.doi.org/10.1016/j.istruc.2020.12.073.
[43] Civera M, Mugnaini V, Zanotti Fragonara L. Machine learning-based automatic operational modal analysis: A structural health monitoring application to masonry arch bridges. Struct Control Health Monit 2022;29(10):e3028. http://dx.doi.org/10.1002/stc.3028.
[44] Brandt A. Single-input frequency response measurements. In: Noise and Vibration Analysis. John Wiley & Sons, Ltd; 2011, p. 285–322. http://dx.doi.org/10.1002/9780470978160.ch13.
[45] Juang J-N, Pappa RS. An eigensystem realization algorithm for modal parameter identification and model reduction. J Guid Control Dyn 1985;8(5):620–7. http://dx.doi.org/10.2514/3.20031.
[46] Grafe H. Model updating of large structural dynamics models using measured response function. Department of Mechanical Engineering, Imperial College; 1999.
[47] Brownjohn JM. Energy dissipation from vibrating floor slabs due to human-structure interaction. Shock Vib 2001;8(6):315–23.
[48] ISO. ISO 5982:1981 vibration and shock - mechanical driving point impedance of the human body. International Organization for Standardization; 1981.
[49] Matsumoto Y, Griffin M. Mathematical models for the apparent masses of standing subjects exposed to vertical whole-body vibration. J Sound Vib 2003;260(3):431–51. http://dx.doi.org/10.1016/S0022-460X(02)00941-0.
[50] Zheng X, Brownjohn JMW. Modeling and simulation of human-floor system under vertical vibration. In: Davis LP, editor. Smart structures and materials 2001: smart structures and integrated systems, Vol. 4327. SPIE, International Society for Optics and Photonics; 2001, p. 513–20. http://dx.doi.org/10.1117/12.436586.
[51] Tubino F, Pagnini L, Piccardo G. Uncertainty propagation in the serviceability assessment of footbridges. Struct Infrastruct Eng 2020;16(1):123–37. http://dx.doi.org/10.1080/15732479.2019.1618879.
[52] Ellirtgwood B. Design and construction error effects on structural reliability. J Struct Eng 1987;113(2):409–22. http://dx.doi.org/10.1061/(ASCE)0733-9445(1987)113:2(409).
[53] Kareem A, Gurley K. Damping in structures: Its evaluation and treatment of uncertainty. J Wind Eng Ind Aerodyn 1996;59(2):131–57. http://dx.doi.org/10.1016/0167-6105(96)00004-9.
[54] Van Nimmen K, Lombaert G, De Roeck G, Van den Broeck P. Vibration serviceability of footbridges: Evaluation of the current codes of practice. Eng Struct 2014;59:448–61. http://dx.doi.org/10.1016/j.engstruct.2013.11.006.
[55] Moser P, Moaveni B. Environmental effects on the identified natural frequencies of the Dowling Hall Footbridge. Mech Syst Signal Process 2011;25(7):2336–57. http://dx.doi.org/10.1016/j.ymssp.2011.03.005.
[56] Pagnini L. Model reliability and propagation of frequency and damping uncertainties in the dynamic along-wind response of structures. J Wind Eng Ind Aerodyn 1996;59(2):211–31. http://dx.doi.org/10.1016/0167-6105(96)00008-6.
[57] Pagnini L. Reliability analysis of wind-excited structures. J Wind Eng Ind Aerodyn 2010;98(1):1–9. http://dx.doi.org/10.1016/j.jweia.2009.08.010.
[58] Pagnini L, Repetto MP. The role of parameter uncertainties in the damage prediction of the alongwind-induced fatigue. J Wind Eng Ind Aerodyn 2012;104–106:227–38. http://dx.doi.org/10.1016/j.jweia.2012.03.027, 13th International Conference on Wind Engineering.
[59] Živanović S, Pavić A, Reynolds P. Probability-based prediction of multi-mode vibration response to walking excitation. Eng Struct 2007;29(6):942–54. http://dx.doi.org/10.1016/j.engstruct.2006.07.004.
[60] Živanović S, Pavia A. Probabilistic assessment of human response to footbridge vibration. J Low Freq Noise Vib Act Control 2009;28(4):255–68. http://dx.doi.org/10.1260/0263-0923.28.4.255.
[61] Tubino F. Probabilistic assessment of the dynamic interaction between multiple pedestrians and vertical vibrations of footbridges. J Sound Vib 2018;417:80–96. http://dx.doi.org/10.1016/j.jsv.2017.11.057.
[62] Santoro R, Sofi A, Tubino F. Serviceability assessment of footbridges via improved interval analysis. ASCE-ASME J Risk and Uncert Eng Syst B Mech Eng 2021;7(2):020906. http://dx.doi.org/10.1115/1.4050169.